



Solar Flare Arcade Modeling: Bridging the Gap from 1D to 3D Simulations of Optically Thin Radiation

Graham S. Kerr^{1,2,5} , Joel C. Allred¹ , and Vanessa Polito^{3,4} 

¹NASA Goddard Space Flight Center, Heliophysics Sciences Division, Code 671, 8800 Greenbelt Rd., Greenbelt, MD 20771, USA; graham.s.kerr@nasa.gov

²Department of Physics, Catholic University of America, 620 Michigan Avenue, Northeast, Washington, DC 20064, USA

³Bay Area Environmental Research Institute, NASA Research Park, Moffett Field, CA 94035-0001, USA

⁴Lockheed Martin Solar and Astrophysics Laboratory, Building 252, 3251 Hanover Street, Palo Alto, CA 94304, USA

Received 2020 June 15; revised 2020 July 20; accepted 2020 July 27; published 2020 August 27

Abstract

Solar flares are 3D phenomena, but modeling a flare in 3D, including many of the important processes in the chromosphere, is a computational challenge. Accurately modeling the chromosphere is important, even if the transition region and corona are the areas of interest, due to the flow of energy, mass, and radiation through the interconnected layers. We present a solar flare arcade model that aims to bridge the gap between 1D and 3D modeling. Our approach is limited to the synthesis of optically thin emission. Using observed active region loop structures in a 3D domain, we graft simulated 1D flare atmospheres onto each loop, synthesize the emission, and then project that emission onto the 2D observational plane. Emission from SDO/AIA, GOES/XRS, and IRIS/SG Fe XXI λ 1354.1 was forward modeled. We analyze the temperatures, durations, mass flows, and line widths associated with the flare, finding qualitative agreement but certain quantitative differences. Compared to observations, the Doppler shifts are of similar magnitude but decay too quickly. They are not as ordered, containing a larger amount of scatter compared to observations. The duration of gradual phase emission from GOES and AIA emission is also too short. Fe XXI lines are broadened, but not sufficiently. These findings suggest that additional physics is required in our model. The arcade model that we show here as a proof of concept can be extended to investigate other lines and global aspects of solar flares, providing a means to better test the coronal response to models of flare energy injection.

Unified Astronomy Thesaurus concepts: [Solar flares \(1496\)](#); [Solar flare spectra \(1982\)](#); [Active solar corona \(1988\)](#); [Solar x-ray flares \(1816\)](#); [Hydrodynamical simulations \(767\)](#); [Solar radiation \(1521\)](#); [Solar ultraviolet emission \(1533\)](#); [Radiative transfer simulations \(1967\)](#)

Supporting material: animations

1. Introduction

Magnetic reconnection in the solar corona can liberate a tremendous amount of magnetic energy. The released energy can intensely heat and ionize the solar atmosphere, leading to a broadband enhancement to the solar radiative output, known as a solar flare. This same process can result in the production of coronal mass ejections (CMEs) and solar energetic particles (SEPs). Flares, CMEs, and SEPs drive geoeffective space weather, making understanding the various physical processes involved in energy release and transport of crucial importance. Here we focus on the solar flare component, presenting a new approach to model the coronal flare arcade with radiation hydrodynamic modeling.

Following reconnection, energy is transported along the legs of magnetic loops. In the standard flare model energy is carried by a beamed distribution of nonthermal electrons accelerated out of the ambient corona, which undergo Coulomb collisions, thermalizing the electrons in the chromosphere or transition region (Brown 1971; Holman et al. 2011). The sudden temperature increase leads to expansion of chromospheric material up into the corona (“chromospheric ablation,” also referred to as “evaporation”; Fisher et al. 1985a, 1985b) and down into the deeper atmosphere (“chromospheric condensation”; Fisher 1989). Energy transport via nonthermal particles

and thermal conduction are field-aligned processes. The resulting dynamics of the flaring plasma are also field aligned, constrained by the magnetic field.

Plasma heating, ionization, mass flows, and other physical properties reveal themselves through the emission of both continuum and spectral line radiation from the various layers of the solar atmosphere (Fletcher et al. 2011; Milligan 2015). Optical and ultraviolet (UV) emission typically appear in ribbon-like sources, which show substructure, and are due to thermal plasma processes. Hard X-ray emission appears as compact footpoint sources at the base of magnetic loops and presents unambiguous evidence of particle acceleration in flares. Soft X-ray emission is somewhat delayed relative to the hard X-ray peak and appears in flare loops and loop tops once the density has increased sufficiently following ablation. Extreme-ultraviolet emission appears in both footpoint and loop sources and usually indicates the presence of high-temperature plasma. See Fletcher et al. (2011), Holman et al. (2011), Kontar et al. (2011), and Holman (2016) for reviews of flare observations and physical processes.

As reconnection progresses, energy is deposited into new loops. Ribbons spread both along and away from the polarity inversion line (e.g., Grigis & Benz 2005; Qiu et al. 2010, 2017; Cheng et al. 2012), and loops brighten, so that a flare arcade forms. A quintessential example of a flare arcade is the Bastille Day flare (see images in Fletcher & Hudson 2001; Holman 2016). The arcade structure means that along the line of sight

⁵ Work began while a NASA Postdoctoral Program (NPP) Fellow, administered by USRA.

we are potentially detecting radiation from multiple ribbons, footpoints, loops, and loop tops.

Through comparisons of synthetic observables derived from numerical models of flares we can determine if our models of energy transport and the atmospheric response are sufficient, or if additional ingredients are required. For example, do we need to consider the presence of turbulence, nonthermal ions, Alfvénic waves, or more sophisticated treatments of the electron beam?

The small spatial scales involved in shocks and steep gradients demand high resolution in numerical models that include an accurate chromosphere and transition region (Abbett & Hawley 1999; Allred et al. 2005; Bradshaw & Cargill 2013). Simulations that model the chromosphere’s response to a beam of energetic particles, with non-LTE (NLTE), nonlocal radiation transport and time-dependent atomic level populations (that are coupled to the equations of hydrodynamics via radiative losses in the energy conservation equation), in 3D are currently a computationally difficult (if not intractable) problem. An advanced 3D radiation magnetohydrodynamic model of a flare was recently performed by Cheung et al. (2019). While this impressive achievement managed to model reconnection, the structure of flaring magnetic loops, and energy release in an active region, leading to heating equivalent to a C-class flare (determined from the flux of forward-modeled soft X-rays), it did not include nonthermal particle acceleration and their resulting energy deposition profile. Energy transport was solely via thermal conduction in their model.

Since both energy transport and dynamics within the flare loop are field-aligned processes, we note (and stress) that the 1D modeling approach is actually a reasonable assumption, allowing us to include more detailed physics than would be possible in 3D modeling.

Magnetic-field-aligned (1D) loop models of solar flares have thus emerged as vital tools to understand the various aspects of the flare problem, including the response of the atmosphere to nonthermal electron beam heating (examples include Abbett & Hawley 1999; Allred et al. 2005, 2015; Kašparová et al. 2009; Reep et al. 2013), investigating alternative energy transport techniques (examples include Kerr et al. 2016; Reep & Russell 2016; Reep et al. 2016a, 2018b; Polito et al. 2018; Procházka et al. 2018), and understanding the detailed formation processes of various observables to aid in the interpretation of observations (Kowalski et al. 2015, 2017; Brown et al. 2018; Kerr et al. 2019a, 2019b, 2019c; Zhu et al. 2019; Graham et al. 2020).

The impact of omitting optically thick 3D radiation transfer effects (such as radiative heating and cooling) in flares is not well known and is beyond the scope of this current study. We do know, though, that the 3D nature of flaring structures is important to consider when either interpreting or modeling optically thin emission, since emission is summed along the line of sight.

When studying emission from the chromosphere or transition region and performing model–data comparisons, it suffices to treat the vertical extent of the 1D model’s upper chromosphere and transition as part of the flare ribbon or footpoint, as these layers are fairly narrow. However, if one is interested in coronal emission from the flare loops, then this simplification is no longer appropriate. A spectral line could form over an extended portion of a hot flare loop, so summing emission through the loop in that manner would not be realistic.

Instead, only portions of the loop should be selected and the line of sight to the observer accounted for.

The technique of Bradshaw & Klimchuk (2011) has been used to model coronal emission in this manner (Bradshaw & Klimchuk 2015; Polito et al. 2016; Reep et al. 2016b, 2018a; Mandage & Bradshaw 2020). In that approach the flare loop simulated is assumed to be semicircular, at disk center, and oriented perpendicular to the solar surface, aligned east–west. The line of sight is parallel to the plane of the loop. The spatial emission along the loop can then be binned into a single row of detector pixels. See Figure 1 in Bradshaw & Klimchuk (2011) for a visual depiction. Another approach to model coronal emission was that of Polito et al. (2019), who used a similar method but included inclination angles of the loops relative to the detector and superposition of several loops.

Here we present our approach to study optically thin flare emission that aims to account for the spatial extent of the loop relative to a detector pixel, loop geometry, inclination, the superposition of loops, and the location on the solar disk. A flare arcade model was produced as a proof of concept, illustrating how we bridge the gap from the state-of-the-art 1D field-aligned detailed loop model of a flare to a data-constrained 3D arcade structure from which emission is forward modeled and then projected onto a 2D observational plane. We use observed loop structures from an active region for this purpose.

Forward modeling of several observables is presented to illustrate how the arcade modeling approach can facilitate model–data predictions and to assess how well the model can reproduce aspects of the flare. Both qualitative and quantitative comparisons are made to observations from the Geostationary Operational Environmental Satellite’s X-ray Sensor (GOES/XRS), the Solar Dynamics Observatory’s Atmospheric Imaging Assembly (SDO/AIA; Lemen et al. 2012; Pesnell et al. 2012), and the Interface Region Imaging Spectrograph’s Spectrograph (IRIS/SG; De Pontieu et al. 2014).

2. RADYN Field-aligned Loop Modeling

The 1D, field-aligned, radiation hydrodynamics code RADYN (Carlsson & Stein 1992, 1997, 2002; Allred et al. 2005, 2015; J. C. Allred et al. 2020, in preparation) models the solar atmosphere’s response to flare energy injection, including the feedback between the nonlocal, NLTE radiation transfer and hydrodynamics. Radiation from hydrogen, helium, and calcium (species important for energy balance) is treated in detail (including nonequilibrium effects), and other species are included via a radiation loss function. It uses an adaptive grid (Dorfi & Drury 1987) to capture shocks and strong gradients that typically form in flares. An important feature of RADYN is its ability to model an accurate chromosphere, which impacts the response of other atmospheric layers and the spatiotemporal evolution of flare energy deposition. Thus, the development of flows and coronal plasma properties are impacted by how the lower atmosphere responds.

Flare energy is injected via a nonthermal electron distribution, with a Fokker–Planck treatment that includes transport effects through the flare loop (Allred et al. 2015; J. C. Allred et al. 2020, in preparation). Thermal conduction is Spitzer with a flux limiter to avoid exceeding the electron free streaming rate (Smith & Auer 1980). It is also possible to inject flare energy via an approximated form of downward-propagating

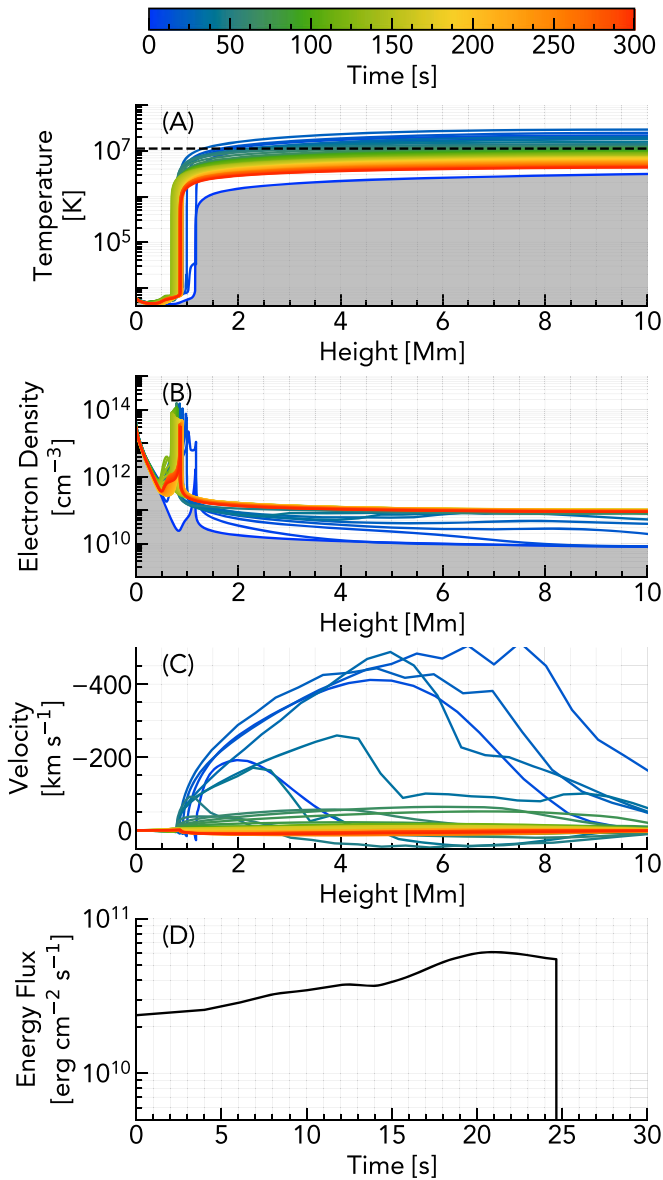


Figure 1. Flare atmospheres (the temperature, electron density, and atmospheric velocity, where upflows are negative, shown in panels (A)–(C), respectively) from RADYN at various times in the simulation. Heating was applied for 25 s (panel (D)). The dashed horizontal line indicates the peak formation temperature of Fe XXI, $T \sim 11.2$ MK.

Alfvénic waves (Kerr et al. 2016), though we do not model those in this work.

RADYN has become a commonly used resource to study both energy transport in flares and the formation of radiation during flares (until recently, typically focusing on chromospheric and transition region radiation). For a more detailed description of the code, and for examples of recent studies using RADYN, consult Allred et al. (2015), Kowalski et al. (2015), Kerr et al. (2019a, 2019c), Polito et al. (2019), and references therein.

The pre-flare atmosphere was one-half of a symmetric loop, spanning the subphotosphere, photosphere, chromosphere, transition region (TR), and corona. Energy was injected at the loop apex. The injected nonthermal electron distribution had flux on the order of $(1\text{--}6) \times 10^{10}$ erg cm $^{-2}$ s $^{-1}$ (the actual injected flux varied in time and is shown in Figure 1) with a spectral index $\delta = 7.2$, above a low-energy cutoff $E_c = 25.3$ keV. Energy was injected for approximately 25 s, after which the flare loop cooled

for several hundred seconds. Figure 1 shows the response of the atmosphere at several snapshots. For the purposes of this experiment combining RADYN and arcade modeling, we selected a preexisting RADYN simulation that had a large amount of plasma at $T > 11$ MK and large mass flows against gravity (upflows), so that we could explore characteristics of the Fe XXI $\lambda 1354.1$ flare line. These parameters lie within the typical range for moderate to strong flares based on RHESSI hard X-ray observations (e.g., Holman et al. 2011). We do not believe that changing these parameters would affect our overall conclusions.

The chromosphere rapidly heats and ionizes, increasing the electron density throughout the lower atmosphere. Explosive chromospheric ablation (upflowing material, commonly referred to as “evaporation”) results, filling in the coronal portion of the loop, producing a hotter and denser corona. The location of the TR during the flare decreases in altitude.

These conditions allow for the presence of highly ionized species and the generation of spectral lines that typically only appear during flares or other transient heating events. RADYN tracks nonequilibrium processes for certain chromospheric species but does not do this as standard for iron. This will feature as a future avenue of investigation, but for this current work we rely on the assumption of equilibrium ionization to obtain the fraction of Fe XXI present in our flare loop.

Following cessation of energy injection, the mass flows decrease, and radiative losses and thermal conduction efficiently cool the corona, which undergoes a rapid catastrophic cooling period.

2.1. Fe XXI $\lambda 1354.1$ Emission from the 1D Model

From the field-aligned model we synthesized Fe XXI light curves. This is appropriate since we are interested in the integrated line intensity. Full line profiles and associated characteristics require imposing a line-of-sight information for the Doppler shifts, which we do in the arcade modeling.

Data from the CHIANTI atomic database (version 8.0.7; Dere et al. 1997; Del Zanna et al. 2015) were used with the physical properties of the plasma to forward model the emissivity of the Fe XXI $\lambda 1354.1$ spectral line in each grid cell. The contribution functions $G(\lambda, n_e, T)$ were built using the standard atomic data in CHIANTI, assuming ionization equilibrium. These were tabulated with a resolution of $\delta \log T = 0.05$ and $\delta \log n_e = 0.5$. In each grid cell $G(\lambda, n_e, T)$ was interpolated to the n_e and T of the plasma, and the emissivity was calculated as

$$\dot{j}_{\lambda,z} = A_{\text{Fe}} G(\lambda, n_e, T) n_e(z) n_{\text{H}}(z), \quad (1)$$

where n_{H} is the hydrogen density and A_{Fe} is the elemental abundance of iron in the solar atmosphere. We used the abundance value from Schmelz et al. (2012), $A_{\text{Fe}} = 7.85$, defined on the usual logarithmic scale, where $A_{\text{H}} = 12$ (the abundance relative to hydrogen, A_{rel} , is obtained using $A_{\text{rel}} = 10^{A_{\log} - A_{\text{H}}}$ for an abundance value expressed on the logarithmic scale, A_{\log}). There is much debate over which abundance value to use for iron and other low first ionization potential (FIP) elements during flares. Coronal abundances of low-FIP elements are enhanced relative to photospheric values. For iron the photospheric abundance is $A_{\text{Fe}} = 7.50$ (Asplund et al. 2009), but the coronal abundance can be as high as $A_{\text{Fe}} = 8.10$ (Feldman 1992). While some studies have shown that in flares the low-FIP elements actually have abundances closer to photospheric (e.g., Warren 2014, since ablation carries

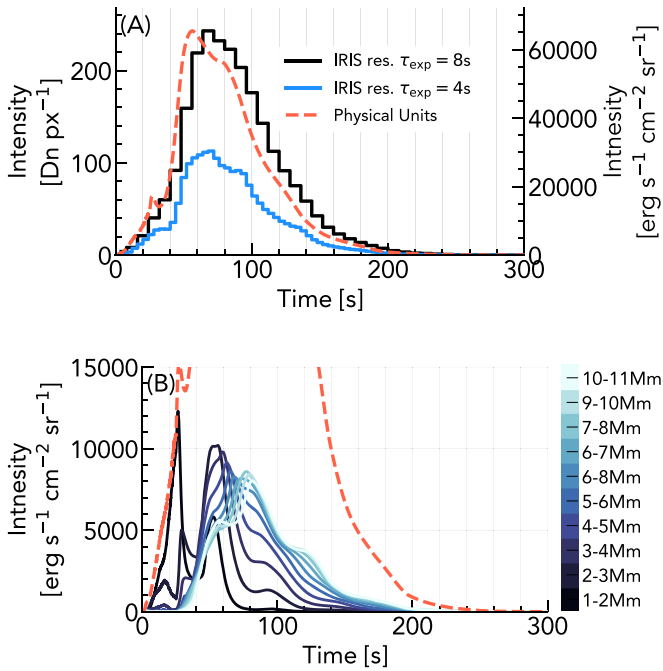


Figure 2. (A) Light curves of the Fe XXI $\lambda 1354.1$ line from the 1D field-aligned model, both at native resolution and with physical units (red dashed line, right-hand axis), and as would be observed by IRIS at two typical exposure times (blue and black solid lines, left-hand axis). These represent emission integrated through the full loop. Panel (B) shows the light curves broken down into height ranges (colored lines), with the total also indicated (red dashed line).

chromospheric material into the flare loop), studies of the iron abundance in flares have produced a range of values $A_{\text{Fe}} = [7.56, 7.72, 7.91, 7.99]$ (Phillips & Dennis 2012; Narendranath et al. 2014; Warren 2014; Dennis et al. 2015). In the latter case the abundance varied in times, and in fact sometimes exceeded the canonical coronal value. We chose the value from Schmelz et al. (2012) as a middle ground and note that the intensity values of the synthetic spectra could be some factor smaller if alternative values of A_{Fe} were used. Our quoted intensities would be a factor $2.2\times$ smaller if the photospheric abundance value from Asplund et al. (2009) were used.

The intensity in each grid cell is then

$$I_{\lambda,z} = j_{\lambda,z} \delta z, \quad (2)$$

where δz is the size of the grid cell. The emergent Fe XXI intensity from either the full 1D field-aligned atmosphere or some range of heights was obtained by summing the intensity in each grid cell along the extent of interest, $I_{\lambda} = \sum_{z_1}^{z_2} I_{\lambda,z}$.

Light curves are shown in Figure 2, both at the native resolution and at IRIS resolution (spectral and temporal resolution, and convolved with the spectrograph effective area), with typical exposure times $\tau_{\text{exp}} = [4, 8]$ s and Poisson noise applied. These illustrate that observations made with longer exposures can obscure dynamics present in the simulation. The emission peaks several tens of seconds following cessation of the electron beam, as the corona takes time to become sufficiently hot and dense to produce the maximum Fe XXI emission. These light curves represent emission summed over the full flare (a single flaring, if observed by IRIS). Also shown in Figure 2 is a breakdown of the intensity within several height ranges, showing that initially the

emission is stronger lower in the atmosphere near the TR, before gaining strength at higher altitudes. During the peak of emission, Fe XXI is forming over an extended range of heights.

3. Modeling the Flare Arcade in 3D

3.1. Data-constrained Identification of Coronal Loops

Allred et al. (2018) performed data-constrained 3D modeling of active region heating via nanoflares, using observations of active region AR 11726 from SDO/AIA, Hinode’s Extreme-ultraviolet Imaging Spectrometer (EIS; Culhane et al. 2007), and the Extreme Ultraviolet Normal Incidence Spectrograph (EUNIS; Brosius et al. 2014). They constructed a 3D model of the magnetic field in AR 11726 using the Vertical Current Approximation Nonlinear Force Free Field (VCA-NLFFF) technique of Aschwanden (2013, 2016). In that approach the photospheric magnetic field from SDO/HMI is extrapolated into the corona, with SDO/AIA observations of observed coronal loops used to ensure that the extrapolated magnetic field lines are co-aligned with actual coronal structures. We summarize some important features here, but full details can be found in Allred et al. (2018).

The 3D magnetic field within a volume that extended $0.5R_{\odot}$ in the Cartesian x - y plane and $1.5R_{\odot}$ in the z plane was obtained, tracing the magnetic field lines passing through each voxel of a $315 \times 315 \times 430$ heliocentric Cartesian grid. A total of 2848 field lines were traced. Area expansion of each loop into the corona was allowed, conserving magnetic flux. The cross-sectional area was defined as $A(s)B(s) = B(s=0)A(s=0)$, for a distance s along the loop. A value of 220 km was assumed for $A(s=0)$ based on recent high-resolution observations (e.g., Kobayashi et al. 2014; Aschwanden & Peter 2017). Within each voxel it is possible for loops to overlap owing to the area expansion. Emission from overlapping loops within a voxel was averaged. Note that RADYN does not currently include area expansion, but this is a planned upgrade to the code.

Allred et al. (2018) applied nanoflare heating to each loop, and the time-averaged radiated emission within each voxel was computed, as was the time-averaged differential emission measure (DEM). DEMs are a commonly used tool to define the amount of material $n_e n_H$ (the electron density and hydrogen density) present in some certain temperature range δT , along the line of sight h : $\text{DEM}(T) = n_e n_H \frac{dh}{dT}$ (with units of $\text{cm}^{-5} \text{K}^{-1}$). Observationally, the DEMs can be derived from multiwavelength observations and are a means to estimate the distribution of plasma within a temperature range.

The heliocentric coordinates of each voxel were projected onto a 2D pixel grid (the observational planes of SDO, EIS, or EUNIS), and the radiated emission or DEM in each voxel was added to the appropriate pixel of the “image.” If multiple voxels (and portions of multiple loops) corresponded to the same pixel, then that emission was summed. In this manner the superposition of loops, the loop geometry, and the viewing angle in the observational plane were all self-consistently accounted for.

Spectral information could then be convolved with instrumental responses to produce synthetic maps of EIS and EUNIS data, and the DEM maps could be convolved with AIA responses to produce synthetic AIA maps. A best-fit time-averaged DEM model of AR 11726 was produced by Allred et al. (2018), from model–data comparisons of their nanoflare simulations to EIS and EUNIS observations.

The 3D magnetic structure (the identified loops) and the observational pixel grid to which they were projected were used by us to construct a flare arcade model. The time-averaged DEM model produced by Allred et al. (2018) was used as our $t = 0$ s, pre-flare, DEM. While this active region did not flare, we took advantage of the existing 3D magnetic field construction to begin our development of, and experiments with, flare arcade modeling. Reproducing the work of Allred et al. (2018) for a flaring active region is a nontrivial task, but future efforts will involve the use of active regions that did flare.

The observational plane pixel grid had a pixel scale of $\delta x = \delta y = 0''.6$ (the AIA pixel scale). Our initial effort kept this same pixel grid even for forward-modeling IRIS observables, as sampling a finer grid would require remaking the voxels with smaller dimensions. While this is desirable, it is a time-consuming process, and for the demonstration of our new approach we believe that keeping the original scaling is sufficient. Future efforts will explore the use of finer grids.

3.2. Synthetic Flare Arcade Model

AR 11726 was located fairly close to the solar limb. To make the line-of-sight projections more straightforward for this initial work, the whole AR was translated by 45° , around the x - z plane, to near disk center. This rotated region is referred to as AR 11726rot and was used to construct a flare arcade model.

A subset of 180 loops were selected from the 2848 loop to form the flare arcade, chosen for their proximity to each other and for their loop lengths that were close to the 20 Mm long RADYN loops (recall that RADYN models one leg of a semicircular loop, so that the total loop length would be 20 Mm, even though we only simulate 10 Mm from photosphere to corona). These loops were ordered by the distance of the loop apex from disk center and activated in groups of $N_{\text{loop}} = 5$ every $\tau_{\text{ac}} = 3$ s starting at $t = 0$ s. Progressing at an arcade simulation cadence of 0.5 s, each voxel of the appropriate loop was filled with either the DEM or the velocity DEM (VDEM; Newton et al. 1995, which simply defines the amount of emission measure (EM) within that has a line-of-sight velocity in the range $v, v + \delta v$) from the RADYN flare simulation. The same RADYN simulation was used for every loop, but since loops were activated at different times, there were various stages of evolution during any one arcade snapshot.

To produce synthetic images and broadband spectral responses (e.g., SDO/AIA or GOES soft X-rays), maps of the DEM in the 2D x - y observational plane were produced. In each arcade snapshot the DEM and the height grid on which it was defined were interpolated from the RADYN simulation to t_{sim} , the arcade simulation time. The arcade loops were described as distance, s , from one footpoint to the other, with 200 cells per loop (the spatial resolution δs varied). For each cell, i , within the loop the temporally interpolated DEMs were spatially interpolated to s_i and s_{i+1} and summed to find the total value in that cell. This was then divided by the distance $\delta s = s_{i+1} - s_i$ to obtain the DEM field (see Equation (5) in Allred et al. 2018, though note in our case that the DEM field is not time averaged). When projected onto the 2D solar x - y observational plane, each cell i may span multiple $[x, y]$ pixels. The pixels to which that cell should be projected were identified, and the DEM field was multiplied by the appropriate line of sight to obtain the DEM. This DEM was summed with

any DEM already projected onto that pixel either from the background or from another loop. The DEM maps $[x, y]$ were then convolved with the instrumental responses as described in Section 4.

To produce synthetic spectra, a similar method was used, with each voxel instead populated by the appropriate VDEM. After interpolating the VDEM between s_i and s_{i+1} the spectrum over a passband $\Delta\lambda$ was computed from the VDEM using Equations (1) and (2). The velocity information of the VDEM was used to Doppler-shift the line where appropriate, and thermal broadening was applied based on the local temperature. Summing the intensity of the spectra between s_i and s_{i+1} provided the total intensity in cell i , $I_{\lambda,i}$. This was divided by δs , to provide the average emissivity in cell i , $j_{\lambda,i}$. The appropriate pixels into which $j_{\lambda,i}$ should be added were identified, and $j_{\lambda,i}$ was multiplied by the “projected height” to yield intensity. As with the DEMs, this intensity was summed with any existing intensity in that pixel. Spectral maps $[\lambda, x, y]$ were then convolved with instrumental responses as described in Section 5.

Summing the DEM or spectra within a pixel means that the projection of structures into the same pixel was taken into account and the effects of superposition of loops (with different velocity fields) are reflected in the output spectra. Both the synthetic images and spectroscopy explicitly assume optically thin conditions, and these methods are not suitable for modeling spectral lines or continua for which opacity is nonnegligible.

Any snapshot of the flare will show loops that were activated at some prior time (and thus at some time through their evolution), some that are newly activated, and some that are yet to be activated, with the progression of the arcade mimicking observations of flares (albeit without ribbon separation in this initial effort). The parameters $N_{\text{loop}} = 5$ and $\tau_{\text{ac}} = 3$ were arbitrarily chosen (on the basis that they produced an M-class flare with soft X-ray light curve that exhibited a quick rise, with slow decay time) for this proof-of-concept, initial experiment, but when simulating a specific event these can be tailored.

For each temperature bin the EM is $\text{EM}(T) = \text{DEM}(T) \times \delta T$, where δT is the bin spacing. Figures 3–5 show maps of the EM summed over various temperature ranges during both impulsive phase and gradual phase (an animated version is available online).

The EMs as functions of temperature are shown in Figure 6 for the full field of view and the subregions (identified in Figure 3). In each case the EM was averaged over the appropriate area and the temporal evolution shown. Plasma in excess of 10 MK is present at the earliest times in the flare, appearing as both loop and footpoint-like sources. Plasma at temperatures >25 MK is present, albeit only for a short time and at low EM. The transition region steepens and narrows during the flare, so that within a pixel of our synthetic observation there is both TR and coronal plasma. Footpoints therefore contain emission spanning tens of thousands to millions of kelvin. Regions with mainly loop or loop top pixels (e.g., panel (D) on Figure 6) show the EM peak at $T > 10$ MK, falling steeply toward lower temperatures. At later times the EM increases in plasma at several MK while material cools. Regions that include footpoints have flatter EMs, with strong emission at cooler temperatures, extending from kK to MK.

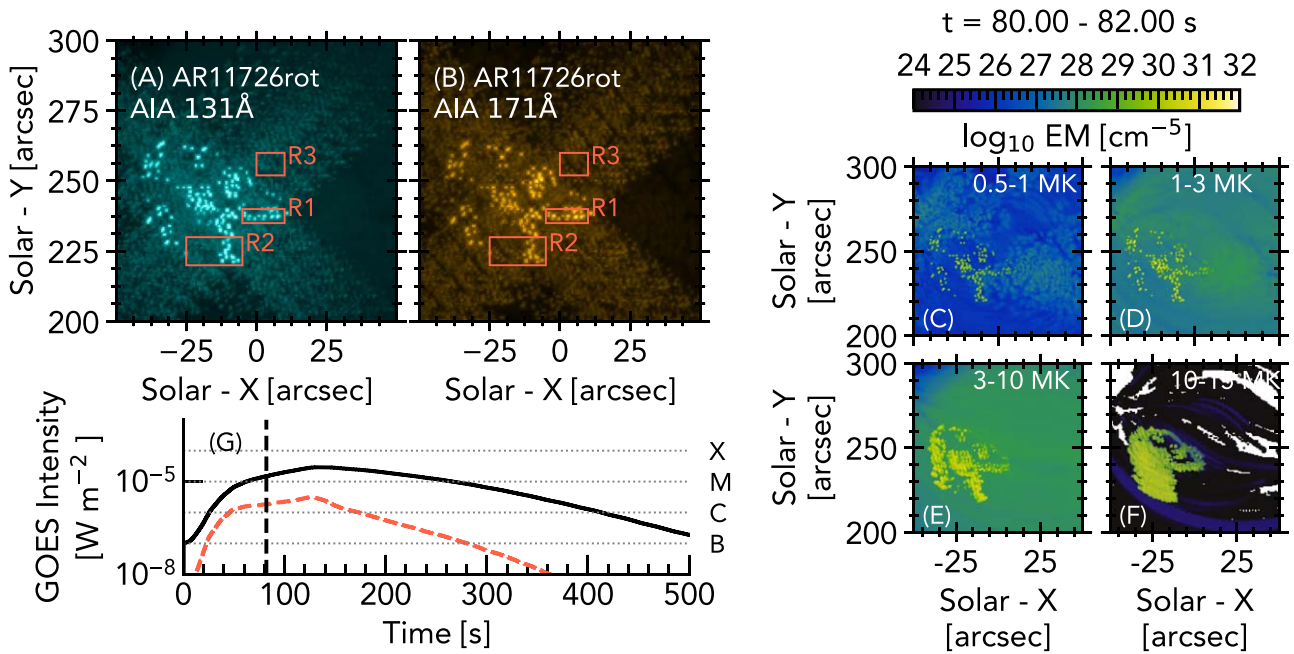


Figure 3. The flare arcade as would be observed by AIA 131 and 171 Å at $t = 80$ s into the flare arcade simulation (panels (A) and (B)), and the EMs summed in various temperature ranges show the structures present at different temperature regimes (panels (C)–(F)). The synthetic GOES 1–8 Å (black) and 0.5–4 Å (orange dashed) light curves are shown in panel (G), where the vertical dashed line indicates the current time and the horizontal lines indicate flare class. The red boxes indicate subregions used to study spatially integrated AIA light curves and EMs. An animated version is available. The video begins in the $t = 0$ –2 s bin and ends in the $t = 548$ –550 s bin. The real-time duration of the video is 55 s.

(An animation of this figure is available.)

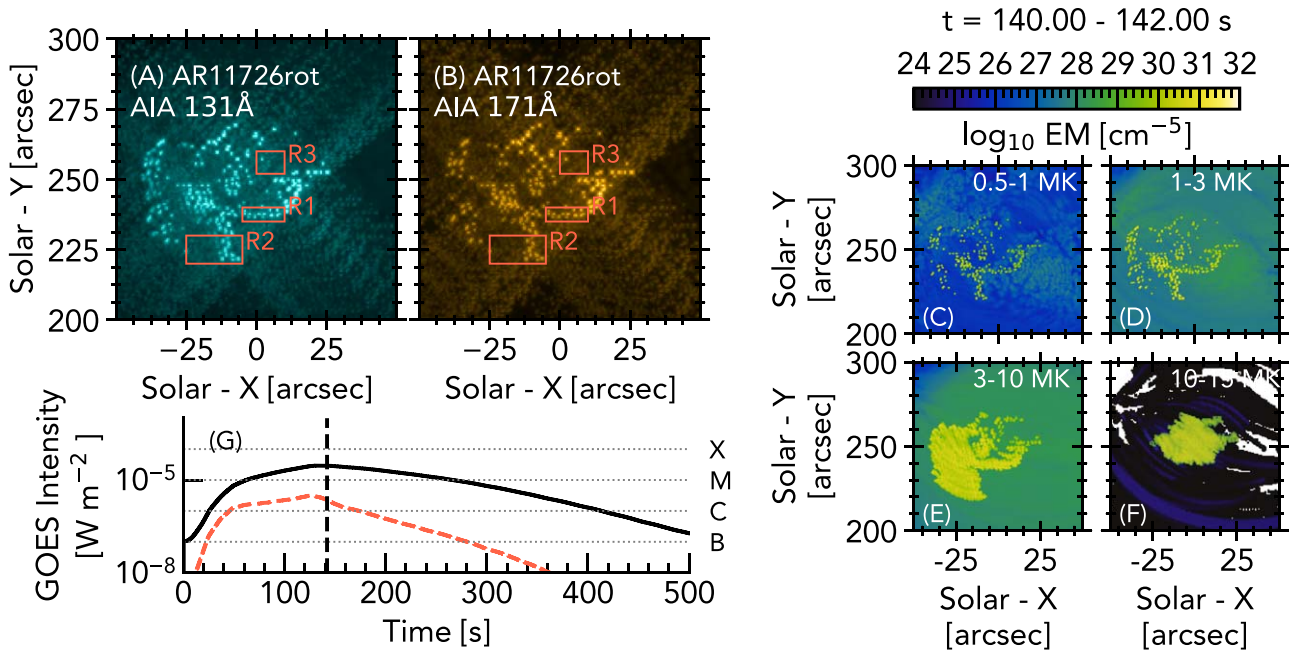


Figure 4. Same as Figure 3, but at $t = 140$ s during the flare model.

4. Synthetic SDO/AIA and GOES Emission

To produce the AIA maps, the DEMs were convolved with the temperature response of the coronal AIA filters. This was done at a cadence of 0.5 s (the cadence at which we progressed the arcade model), with emission assumed to be unchanging over that time period. This provided intensity in $\text{DN s}^{-1} \text{pixel}^{-1}$. Poisson noise was added and the images convolved with the instrumental point-spread function (PSF). Images were integrated over exposure times

of $\tau_{\text{aia}} = 2$ s, so that the final intensity was DN pixel^{-1} . Saturation was not taken into account, and it is likely that in reality these images would suffer from saturation and pixel bleeding effects, which are unfortunately common during flare observations.

Soft X-rays in the [1–8] Å range were synthesized to mimic GOES light curves. For each snapshot, the DEM was integrated over the field of view, with the spatial scale being $\delta x = \delta y = 0''.6$. For each temperature bin the EM was calculated as

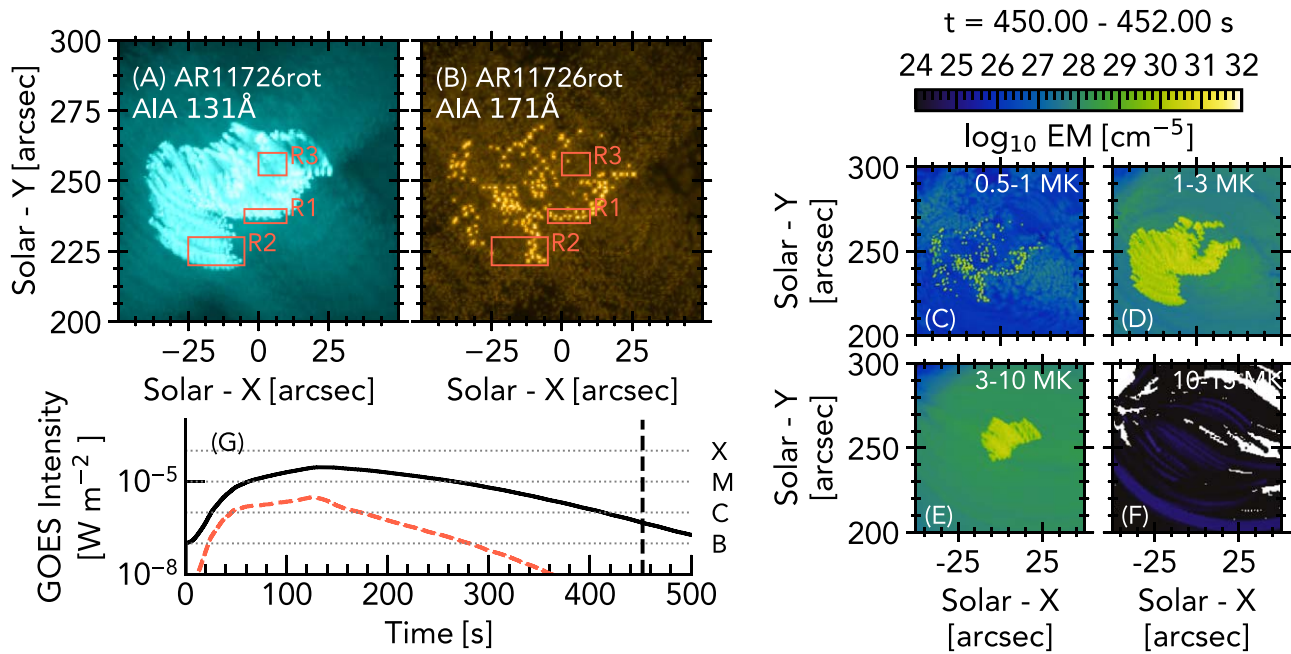


Figure 5. Same as Figure 3, but at $t = 450$ s during the flare model.

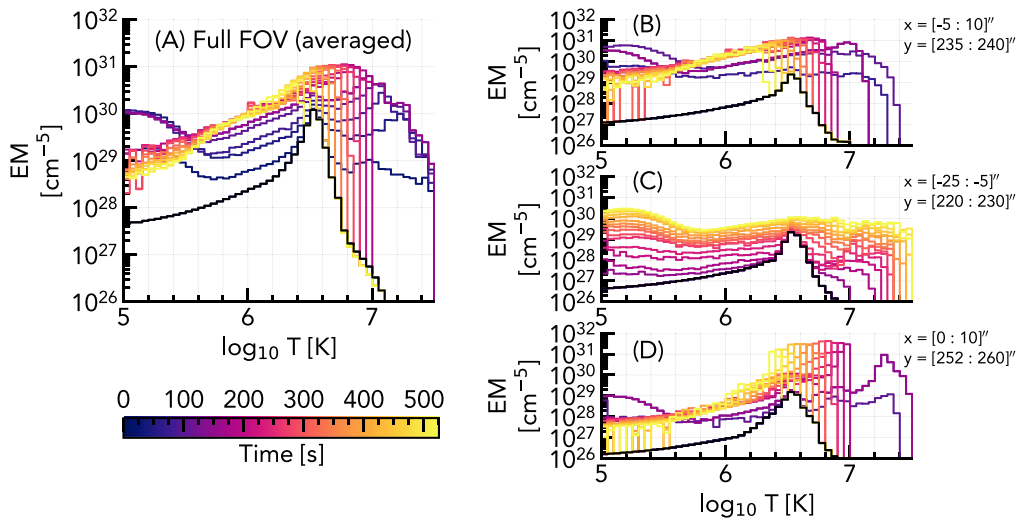


Figure 6. EMs at various times in the arcade simulation. Panel (A) is the full field of view, and panels (B)–(D) are the subregions identified in Figure 3. The black line in each panel is $t = 0$ s.

$EM = DEM \times \delta T$, and the flux of thermal X-rays in the range $E = [1, 50]$ keV (resolution $\delta E = 0.25$ keV) seen at Earth was calculated. This was done using the routine `f_vth.pro` included in the SolarSoftWare package (SSW; Freeland & Handy 1998) and included both lines and continuum. This flux was interpolated to wavelength grids of $[1, 8]$ Å and $[0.5, 4]$ Å, the GOES long and short passbands. Spectra were folded with the GOES-15 spectral response (see White et al. 2005, and `goes_tf_coeff.pro` in the SSW GOES tree). The GOES flux is shown in Figure 3, with the flare peaking at GOES class M2.0 (this is largely a function of the flaring volume, and hence the number of loops we chose to activate in our model, since the same heating rate was applied to each loop).

Maps of the flare as would be observed by AIA 131 and 171 Å are shown in Figures 3–5. The footpoints (“ribbons”) brighten significantly, followed by the loops as they fill with

ablated material. We do not run the simulation past $t = 550$ s, but as the loops cool from >10 MK and material drains from the loops, we would expect the loops to brighten in the channels that probe cooler plasma. Light curves of the full field of view and of several subregions covering footpoint and loop sources are shown in Figure 7. The AIA PSF results in the crosswise effects seen in the images, which artificially results in emission being present in the subregions before the flare actually appeared in those locations. In panels (C) and (E) of Figure 7 there is emission several tens of seconds prior to the peak that is not present if the PSF is not applied. The 131 Å channel peaks somewhat after the cooler channels as the amount of plasma >10 MK increases (this channel also samples cooler emission $T \sim 0.4$ MK). When plasma begins to cool toward the end of the flare, the 94 Å channel peaks, as emission cools from $T > 10$ MK to $T \sim 6$ MK.

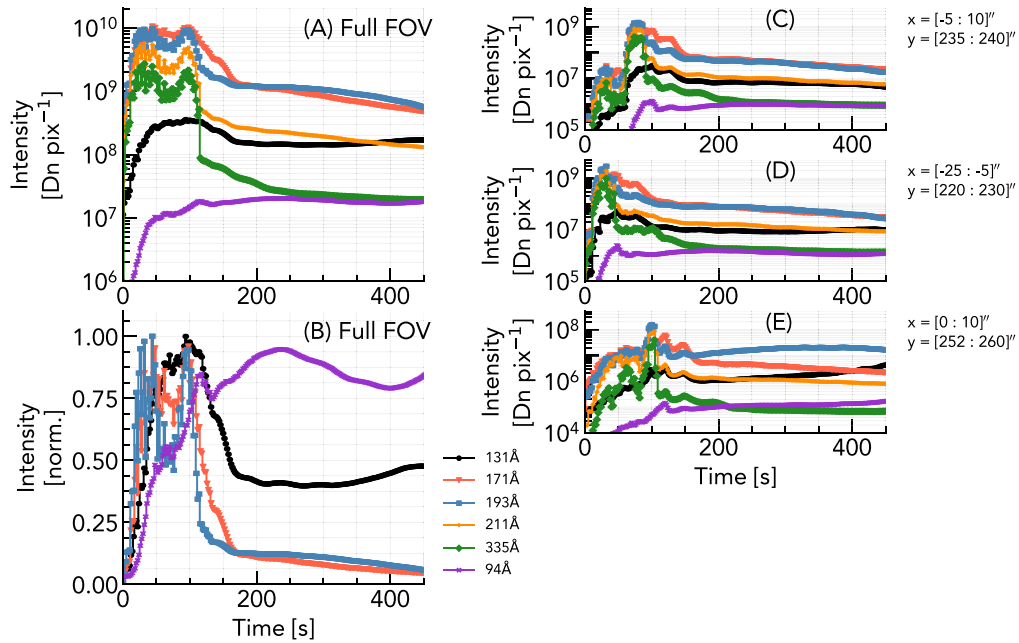


Figure 7. AIA light curves from the arcade simulation. Panels (A) and (B) are the full field of view, and panels (C)–(E) are the subregions identified in Figure 3.

While qualitatively similar to observations from AIA and GOES, the timescales are too rapid in our model. The GOES flare is almost over within ≈ 10 minutes, whereas observed flares have longer lifetimes (e.g., Ryan et al. 2013).

It is common to estimate the (isothermal) temperature of the flaring soft X-ray emission from the ratio of the two GOES channels (e.g., White et al. 2005). Though this isothermal assumption can lead to inaccurate temperatures (e.g., Ryan et al. 2014), this metric is still a useful one for studying the global flare. Studies have investigated flare heating and cooling timescales and characteristics based on these temperatures (e.g., Ryan et al. 2013). Since GOES is a Sun-as-a-star observatory, the observed flux is a combination of both the flare and the disk-integrated emission. It is important, therefore, to remove this background emission before temperatures are derived. Determining this background is not always trivial, and the choice of background can have an impact on the resulting GOES temperatures (e.g., Bornmann 1990; Ryan et al. 2012).

Our flare arcade simulation contains no contamination from background emission, so the temperature derived using our synthetic GOES fluxes ($\mathcal{F}_{\text{flare}}$) represents the flare-only scenario. Of course, GOES observations contain noise and an uncertain background, so to demonstrate the impact of this on our simulated results, we combined our arcade model with actual GOES observations. The 550 s of synthetic GOES fluxes, $\mathcal{F}_{\text{flare}}$, were added to GOES observations from 2013 April 23 17:35 UT, \mathcal{F}_{obs} , shortly after the time of the EUNIS observations, to give a total flux $\mathcal{F}_{\text{tot}} = \mathcal{F}_{\text{flare}} + \mathcal{F}_{\text{obs}}$. Doing this allowed us to include a background level and also permitted us to include variations in the background due to solar sources and noise. Effectively, this is what GOES would have observed, had AR 11726 actually flared. Note that we did not include photon counting statistics or the effects of digitization here (see Simões et al. 2015). The background level to subtract was measured by taking the mean of the GOES fluxes between 2013 April 23 [16–18] UT, $\mathcal{F}_{\text{back}}$.

Temperatures were computed for our arcade model for three cases: $\mathcal{F}_{\text{flare}}$ (no background subtraction necessary),

$\mathcal{F}_{\text{tot}} - \mathcal{F}_{\text{back}}$, and $\mathcal{F}_{\text{tot}} - 1.15\mathcal{F}_{\text{back}}$ (to demonstrate the impact of an uncertain background).

From the appropriate fluxes the temperature was calculated using the SunPy V0.9.10 GOES software (The SunPy Community et al. 2020). Figure 8 shows the temperatures derived from the three cases, along with the GOES light curves. Including the background and variability has a small impact at the start of the event, but overall the behavior is similar to the flare-only “clean” results. In both cases it takes ~ 20 s for the temperature to reach >10 MK and ~ 40 – 50 s to reach the peak of 16.4 MK. The decay is noisier for the case including a background and variability, as would be expected. Increasing the background level does have an impact in the initial stage of the flare. Here the temperature exceeds 10 MK after only 6 s. This may not appear to be a significant difference since the timescales involved are short, but if one is interested in the very start of the flare, then the choice of background can be impactful.

The temporal behaviors of the GOES temperature, SXR flux, and EM in our model are qualitatively consistent with the picture of intense footpoint heating followed by chromospheric ablation that carries material into the flaring loops, increasing their density. The temperature is also consistent with observed GOES temperatures. However, the timescales are too short compared to observations (e.g., Reep & Toriumi 2017; Sadykov et al. 2019). The FWHM was $\tau_{\text{FWHM}} = 149.5$ s, and decay time was $\tau_{\text{decay}} = 99.3$ s, where $\tau_{\text{decay}} = \left. \frac{-F_{1-8 \text{ \AA}}(t)}{dF_{1-8 \text{ \AA}}(t)/dt} \right|_{t=t_{\text{end}}}$, following Reep & Toriumi (2017). While some observations show growth times, decay times, and FWHM on the order of those in our model, Reep & Toriumi (2017) demonstrated that these would imply a ribbon separation close to 3–5 Mm, which is smaller than our model. This discrepancy is likely partly because the individual loops cool too quickly, and partly due to the loop lengths used. Flare SXR timescales are correlated with ribbon separation, which Reep & Toriumi (2017) showed is due to ongoing reconnection and loop expansion so that a range of loop lengths are involved in the flare. Loop length and cooling timescales will be explored with our

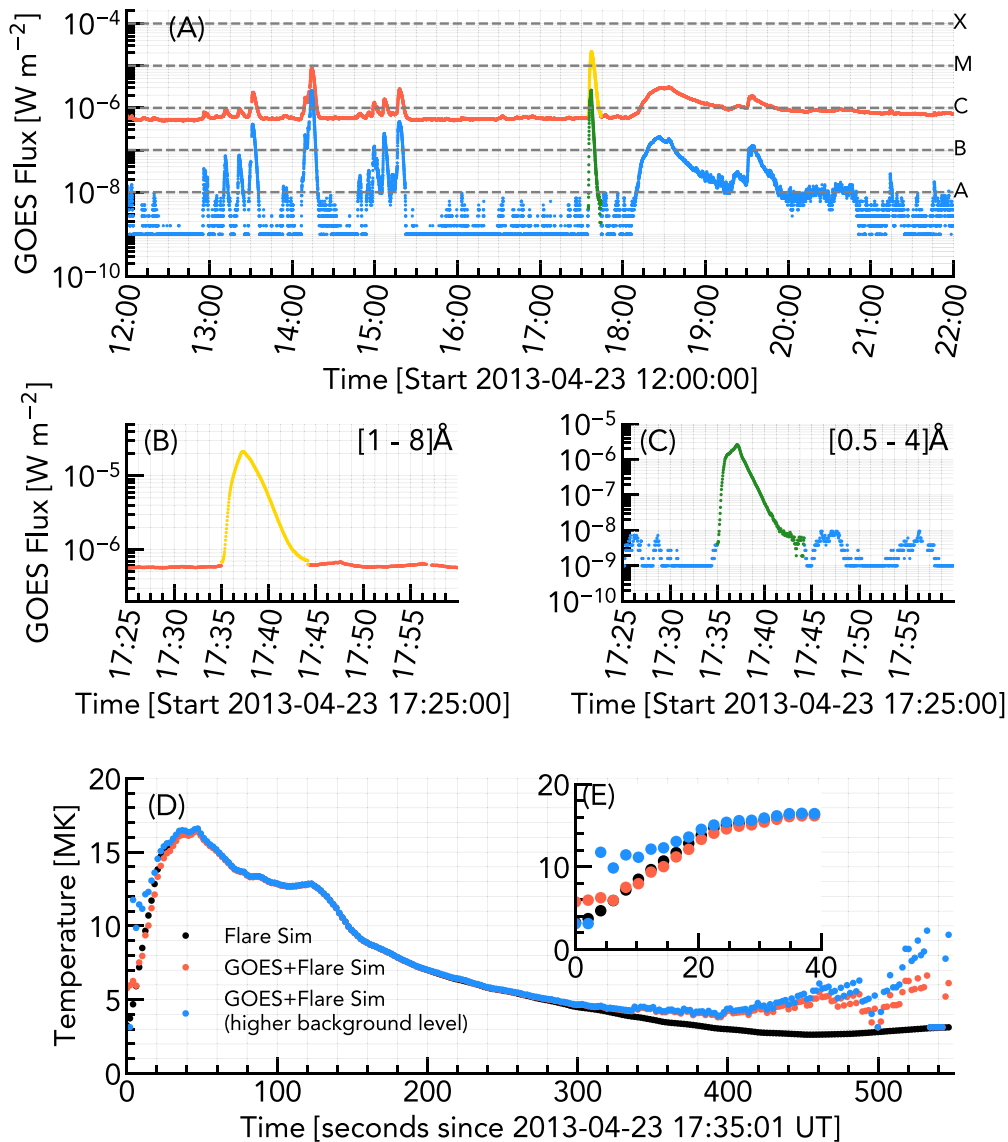


Figure 8. Synthetic GOES SXR emission from the arcade model overlaid on observations from 2013 April 23. Panel (A) shows a 10 hr window of the observed GOES long (red) and short (blue) passbands with the synthetic flare emission added (yellow and green points, respectively). Panels (B) and (C) show a closer look at the time of the modeled flare. Panel (D) shows the derived isothermal temperatures, with the inset panel (E) showing a more detailed view of flare onset. The black points are temperature derived from only the flare simulation, the orange points are from the flare plus observed GOES emission with the average background subtracted, and the blue points are from the same but with a higher background level subtracted.

model in a future work where we attempt to simulate an observed flare arcade.

5. IRIS Fe XXI Emission from the Flare Arcade Model

5.1. Examples of Fe XXI Observations during Solar Flares

In recent years, thanks to the high spectral and spatial resolution afforded by IRIS, Fe XXI $\lambda 1354.1$ emission from flares has been studied in detail to probe flaring plasma properties and dynamics. This high-temperature flare line offers excellent scope to interrogate model predictions of the coronal portion of flare loops. Prior to IRIS this line was observed on disk using Skylab (Doschek et al. 1975) and the UVSP instrument on board the Solar Maximum Mission (Mason et al. 1986). Doppler shifts of up to $\sim 200 \text{ km s}^{-1}$ were seen, line broadening was observed to decrease from flare maximum as the flare progressed, and profiles were usually quite asymmetric. However, owing to limits in spatial resolution, these early results likely suffered from blending

of Fe XXI profiles from multiple sources, creating the asymmetries. With the advantage of improved spectral and spatial resolution, IRIS observations indicated that the Fe XXI profiles were fully blueshifted (with a single component) and showed significant line broadening, with largely symmetric profiles (e.g., Tian et al. 2014, 2015; Graham & Cauzzi 2015; Polito et al. 2015, 2016; Sadykov et al. 2015; Young et al. 2015, and references therein). Generally, the line profiles are observed to initially be weak, strongly blueshifted, broad, and symmetric (Polito et al. 2019). As the flare progresses, they strengthen in intensity, shift toward rest, and narrow. Intensities are around a few tens to a few hundred Data Number (DN) for IRIS exposure times of $\tau_{\text{exp}} \sim 4\text{--}8 \text{ s}$. They first appear in ribbons/footpoints before spreading up loop legs to the loop apex (interpreted as chromospheric ablation). Some observations suggest that Fe XXI sources are offset from the flare ribbon by ~ 0.3 (Young et al. 2015). However, an explanation for this could simply be that the signal is hidden by the bright continuum present in footpoints, so

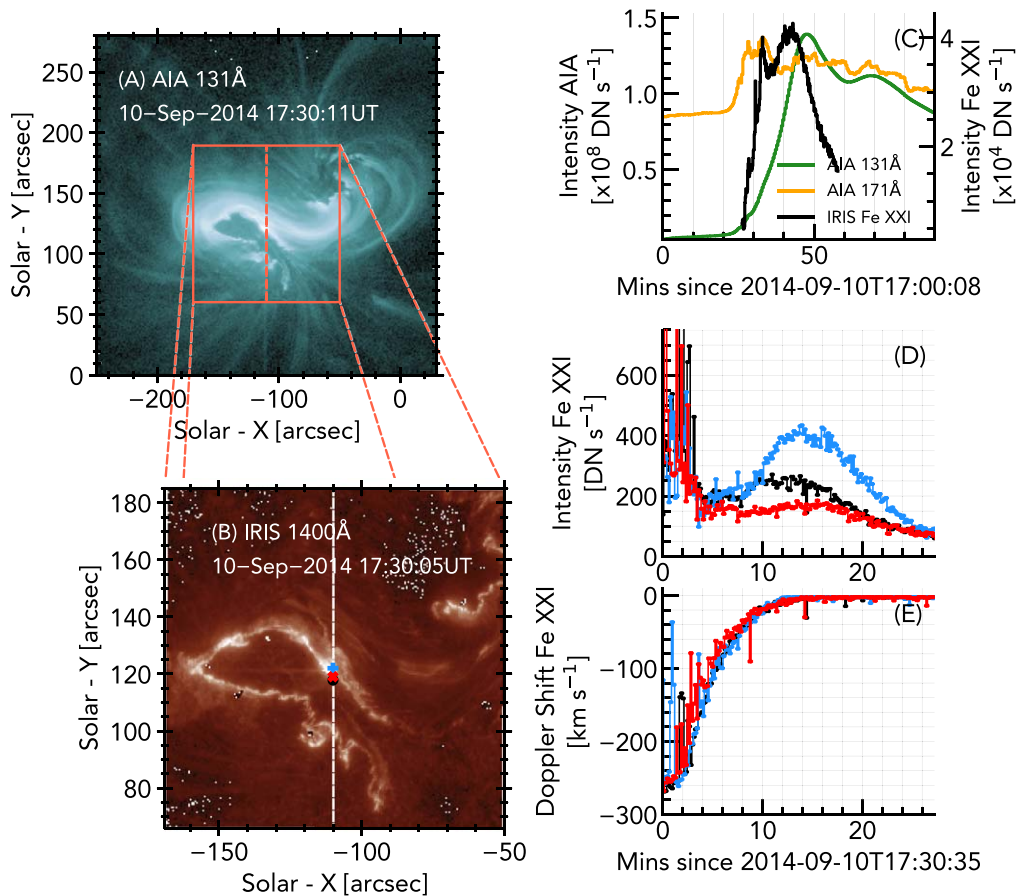


Figure 9. Observations of the 2014 September 10 X-class solar flare. Panel (A) shows AIA 131 Å emission, with the field of view of the IRIS spacecraft indicated (the dashed line is the IRIS slit). Panel (B) shows the IRIS 1400 Å SJI emission. Panel (C) shows the AIA 131 Å (green), AIA 171 Å (orange), and IRIS Fe XXI (black) light curves, integrated over the full field of view. Panel (D) shows the Fe XXI light curves from the pixels indicated in panel (B), and panel (E) shows the Doppler shifts of those same pixels.

that by the first time it is detected the ribbon front has traveled some distance.

Doppler shifts (almost exclusively blueshifts in the impulsive phase ribbons and loops) range from a few tens to 200–300 km s^{-1} and take several hundred seconds to decay from the peak to rest. There is some evidence of small redshifts appearing in the gradual phase owing to draining of flare plasma. Loop tops show profiles that are typically near stationary with negligible broadening. Line widths during the flare range from thermal width (nominally 0.43 Å, assuming ionization equilibrium and a peak formation temperature of 11.2 MK) at loop tops to ~ 0.5 –1 Å in ribbons and loops. The origin of the excess line width is not known with certainty and poses an interesting challenge for modeling to reproduce.

Observations of the 2014 September 10 solar flare are presented in Figure 9, to place the light curves and Doppler shifts from our model in context. Shown in that figure are maps of AIA and IRIS SJI emission, light curves of the full field of view, and the intensity and Doppler shifts of representative pixels. The Fe XXI observations were deblended and fit with a single Gaussian function. This same flare was studied in Graham & Cauzzi (2015) and Polito et al. (2019), and we encourage the reader to consult those sources for a fuller discussion.

Graham & Cauzzi (2015) discovered a strikingly organized behavior of the Fe XXI line Doppler shifts. A superposed epoch analysis of the type performed by Graham & Cauzzi (2015) is

recreated here, to provide a comparison against our modeled superposed epoch analysis presented in Section 5.6. In addition to the Doppler shifts, we present a superposed epoch analysis of the observed line widths also. The temporal origin is defined as the time at which the line first appeared clearly, with a peak of at least 10 DN. This definition is somewhat subjective, as it involved manually assessing movies of each of the 84 pixels used in the analysis. This was a difficult determination owing to the very weak signal when the line first appears, compounded by the fact that it often drifts into the wavelength window of IRIS (meaning that the peak blueshifts quoted here may be lower limits). The temporal binning is $\delta t = 10$ s, and the Doppler shift binning is $\delta v = 10$ km s^{-1} . Note the clustering of Doppler motions, shown in Figure 10(a), and the smooth decay to rest over several hundred seconds. This is less tightly clustered than Graham & Cauzzi (2015), likely due to a stricter determination of when the profile first appeared by Graham & Cauzzi (2015). We find that some pixels exhibit a brief rise phase.

Figure 10(b) shows the analysis applied to the observed line widths. The widths quoted here are the FWHM obtained from Gaussian fitting ($W = 2\sqrt{2 \ln 2} \sigma$, for standard deviation of the Gaussian function σ), a combination of thermal width, instrumental width, and nonthermal width. In order to estimate the nonthermal widths, one should subtract 0.43 Å from the total widths. A line width binning of $\delta W = 12.5$ mÅ was used. At first some pixels show very little broadening (which we

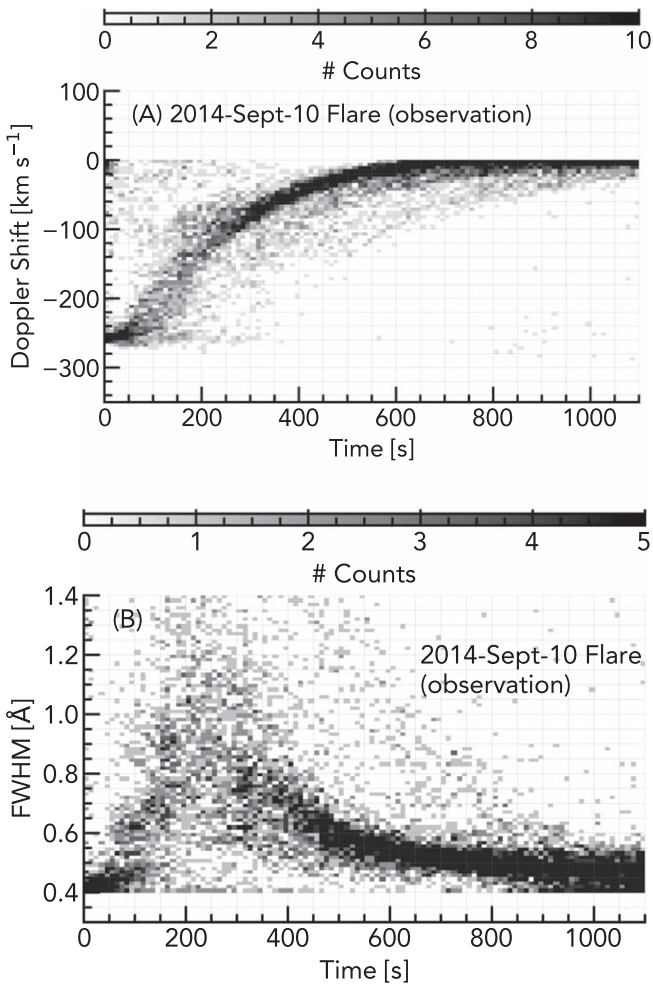


Figure 10. A superposed epoch analysis was applied to results from Gaussian fits to Fe XXI line profiles observed during the 2014 September 10 X-class solar flare. Panel (A) shows the temporal evolution of Doppler shifts ($\delta t = 10$ s, $\delta v = 10$ km s $^{-1}$). Panel (B) shows the line widths, defined as the FWHM of the Gaussian fits ($\delta t = 10$ s, $\delta W = 12.5$ mÅ). The temporal origin of each pixel in both cases was the time of first detection.

believe might be due to the fact that only partial profiles are detected initially, meaning that the widths are underestimated), while others showed significant broadening with a large range of values present. In general, there is more scatter in the line width distribution compared to Doppler shifts.

5.2. Forward Modeling IRIS Spectral Lines

In our arcade model, the Fe XXI $\lambda 1354.1$ line was synthesized over the passband [1352–1356] Å using the approach described in Section 3.2. Particularly in footpoint sources, the continuum is strongly enhanced during flares, which can drown out the Fe XXI signal. To account for this effect, we included the continuum in each cell. The continuum for the background AR was taken from the output of the RH radiative transfer code (Uitenbroek 2001), solving for the FALC semi-empirical model atmosphere (Fontenla et al. 1993). For the flare continuum, the contribution function to the emergent intensity, C_λ , $\mu(z)$ (Magain 1986; Carlsson 1998), was computed. The integral of C_λ , $\mu(z)$ through height is the emergent intensity. Included in C_λ , $\mu(z)$ are various sources of emissivity, attenuated by optical depth. The sources of emissivity included here are various H processes (e.g., free-bound, free-free, H $^-$), scattering processes (e.g., Rayleigh, Thomson),

and background metals (in LTE). See Kowalski et al. (2015, 2017) and G. S. Kerr et al. (2020, in preparation) for further discussion of calculating continuum contribution functions. In each cell of the flaring loops C_λ , $\mu(z)$ was interpolated to the appropriate time and position and added to the emissivity before projecting into pixel $[x, y]$. This is appropriate, as the continuum at these wavelengths is optically thin.

Spectra were converted from I_{erg} (erg s $^{-1}$ cm $^{-2}$ sr $^{-1}$ Å $^{-1}$) to I_{phot} (photons s $^{-1}$ cm $^{-2}$ sr $^{-1}$ Å $^{-1}$), $I_{\text{phot}} = I_{\text{erg}} \frac{\lambda}{hc}$, and an exposure time of $\tau_{\text{exp}} = 4$ s was applied. Multiplying by the solid angle per pixel as viewed at 1 au, smoothing with a spectral PSF (assumed to be a Gaussian with FWHM of two FUV wavelength pixels, $\delta\lambda = 12.98$ mÅ pixel $^{-1}$; De Pontieu et al. 2014), multiplying by the IRIS effective area (calculated for 2014 September 10), and multiplying by the spectral dispersion, provided intensity in photons pixel $^{-1}$. A background level of $B_{\text{DN}} = 0.5$ DN s $^{-1}$ pixel $^{-1}$ (De Pontieu et al. 2014) was converted to photon pixel $^{-1}$, $B_{\text{phot}} = 4B_{\text{DN}}\tau_{\text{exp}}$, where the factor is the number of photons DN $^{-1}$ (De Pontieu et al. 2014), and added to each exposure. Poisson noise was added and the intensity converted to DN pixel $^{-1}$.

The 3D magnetic field structure obtained by Allred et al. (2018) and used by us here was originally designed to be projected onto an x - y grid with pixel size equal to that of SDO/AIA: 0.6 pixel $^{-1}$. In order to obtain IRIS plate scales (0.167 pixel $^{-1}$), we would be required to recreate the analysis of Allred et al. (2018) using smaller voxel dimensions, a nontrivial exercise. Since this initial experiment is largely intended as a demonstration and proof of concept, we have decided to keep the grid from Allred et al. (2018). Future efforts to model a specific flare will use the actual plate scale of the observations.

5.3. Synthetic Fe XXI Line Profiles, Intensities, and Temporal Evolution

Figure 11 shows a snapshot of synthetic IRIS Fe XXI from AR 11726rot. The maps are the emission integrated over the whole passband (1352–1356 Å; recall that this is solely Fe XXI plus continuum since we only generated emission from a single ion in this instance). Spectra from four representative slit positions show the varying intensities, widths, asymmetries, and flows that result from different sources in the arcade. An animated version is available online. When the slit intersects a footpoint source, the continuum brightens significantly. This can obscure the Fe XXI signal, though it is possible to discern its presence in some pixels. When the continuum source decreases in intensity, the Fe XXI emission is much clearer. By this time the brightest continuum source in the footpoints has moved spatially along the slit. The Fe XXI appears offset from the ribbon front for this reason. In some sources the Fe XXI lines are easier to detect in the initial stages and a brief drift toward maximum Doppler shift is visible. These profiles are generally very weak (a few DN pixel $^{-1}$), and so the signal may become vanishingly small in real observations owing to additional noise or the effect of spatial PSFs.

Figure 12 shows individual line profiles from six pixels in AR 11726rot (covering sources at footpoints, loop tops, and on the loops). For each pixel, profiles from exposures 0–60 are shown in steps of two (effective cadence is then 8 s), and the zoomed-in segment is included to make the weaker profiles easier to discern. An animated version is available online. Profiles are initially blueshifted and broad. Though sometimes

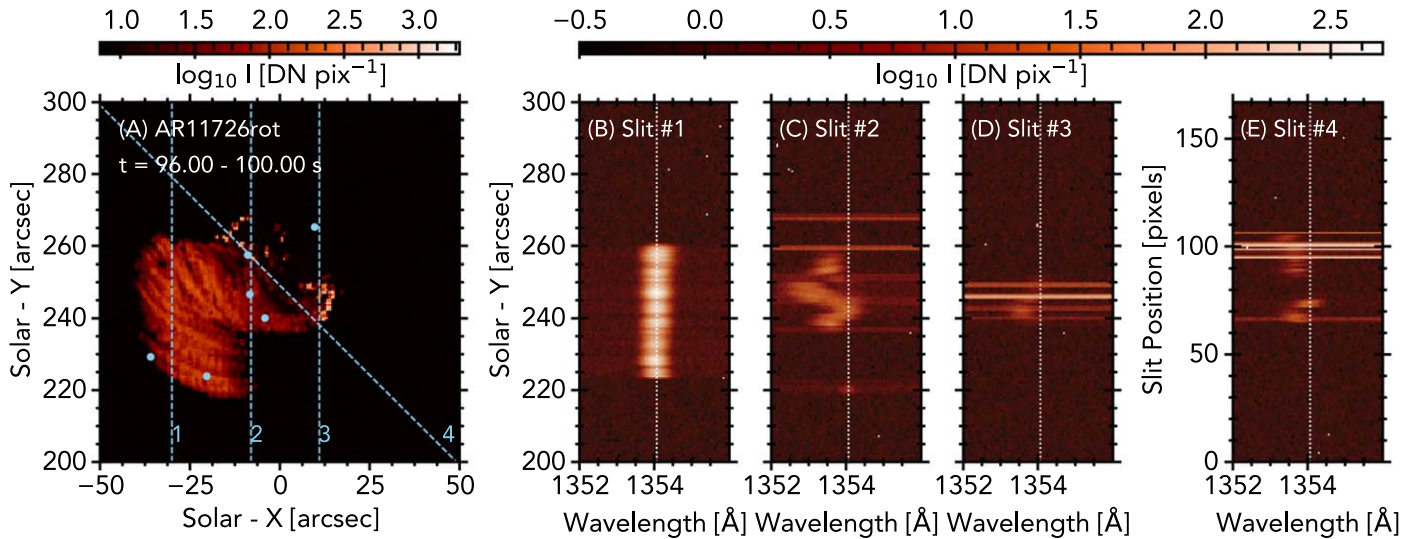


Figure 11. Flare arcade AR 11726rot at $t = 98 \pm 2$ s. Panel (A) is a map of synthetic Fe XXI emission, integrated over 1352–1356 Å, showing footpoint and loop flare sources at various stages of temporal evolution. The blue points indicate the sources for which the spectra are shown in Figure 12. Panels (B)–(E) show Fe XXI from slits 1–4, respectively. Data have been degraded to IRIS resolution as described in the text, had Poisson noise applied, and were integrated with an exposure time of 4 s. The broadband enhancement is caused by a strong flare continuum in the footpoint sources. An animation of this figure is available. The video begins in the $t = 0$ –4 s bin and ends in the $t = 296$ –300 s bin. The real-time duration of the video is 15 s.

(An animation of this figure is available.)

symmetric, asymmetries are present. Over time the profiles drift back toward rest, increasing in strength, becoming narrower and more symmetric. The characteristics and temporal evolution of the line profiles are qualitatively similar to the behavior seen in observations (with the exception of asymmetric profiles). The simulated intensities are of the correct magnitude compared to IRIS observations, suggesting that the temperatures and densities present in the model are consistent with the real flaring plasma.

Figure 13 shows in more detail the source at pixel $x = [-4.10, 240.05]''$, including the light curves of intensity and Doppler shift. The profile rapidly becomes blueshifted but decays to rest over a short period of time of the order ~ 30 s. Recall that the heating timescale was $t = 25$ s. The lifetime of this source, from brightening to returning to near background level, is on the order of 100 s. This is shorter than the monolithic loop light curves (Figure 2), where the lifetime was closer to 200 s.

Light curves of the full field of view and of several subregions are shown in Figure 14. Synthetic light curves of subregions containing footpoint emission (R1 and R2; red and blue curves) are qualitatively similar to the observed Fe XXI light curve shown in Figure 9(c), which also contains footpoint emission. These exhibit a double-peaked structure, the first peak being the footpoint sources low in the loop, and the second peak being due to ablation into the loop producing emission there. The region containing mainly loop or loop top sources (R3; orange line in Figure 14) only exhibits one peak.

5.4. Synthetic Fe XXI Doppler Shifts

To extract properties of the line profiles, Gaussian fits were made to the synthetic data. A single Gaussian function was fit to every pixel to determine the centroid, λ_c , peak intensity, and standard deviation, σ . Photon counting noise was considered in each fit. A five-term Gaussian function (background level with linear component, amplitude, centroid, and standard deviation)

was fit, to account for variations due to the continuum. The number of pixels ($251 \times 251 \times 75 = 4,725,075$ pixels for the 4 s exposure data) precluded manually checking the quality of fit results, and so any fit with $\chi^2 > 2$ or peak intensity $I_{\text{peak}} < 5$ DN pixel $^{-1}$ was omitted so as to avoid spurious data. Where $\chi^2 > 2$, a double-Gaussian function was fit in case the single-Gaussian fit was unsuccessful owing to the presence of multiple components. Only a small proportion of pixels were deemed to be better fit by a double-Gaussian function: 1.6% in AR 11726rot $\tau_{\text{exp}} = 4$ s, and 2.2% in AR 11726rot $\tau_{\text{exp}} = 8$ s. A somewhat larger proportion of longer-exposure ($\tau_{\text{exp}} = 8$) profiles exhibited double components, likely due to temporal smearing of profiles along the line of sight. Further, these profiles typically appeared when loops were more tightly clustered.

Doppler shift(s) of the profiles were computed by $v_{\text{Dopp}} = c (\lambda_c - \lambda_{\text{rest}}) / \lambda_{\text{rest}}$ for speed of light c and rest wavelength $\lambda_{\text{rest}} = 1354.0665$ Å, the rest wavelength in CHIANTI v8.07, used for spectral synthesis in our arcade model. Note that while the rest wavelength has been suggested to be closer to 1354.1 Å (Young et al. 2015), based on IRIS observations, the CHIANTI value is still $\lambda_{\text{rest}} = 1354.0665$ Å.

For most of the duration of the flare in the RADYN simulation, plasma at temperatures that can form Fe XXI exhibits mass flows acting against gravity. That is, mass motions are upflows along the flare loops that would be expected to produce blueshifted emission. Of course, the magnitude of this inferred flow would be modified by the inclination of loops and viewing angles.

Both sides of the arcade model show blueshifted emission during the impulsive phase of each loop. Figure 15 shows several snapshots of the Doppler shift of the Fe XXI $\lambda 1354.1$ line. The integrated intensity of Fe XXI is shown in each panel for context (intensity is scaled by $I^{1/4}$, and image $\alpha = 0.1$). Generally the strongest blueshifts are present around the edge of the flaring structure, and hence the footpoints of the loops, weakening with height along the loops. Flows appear first at

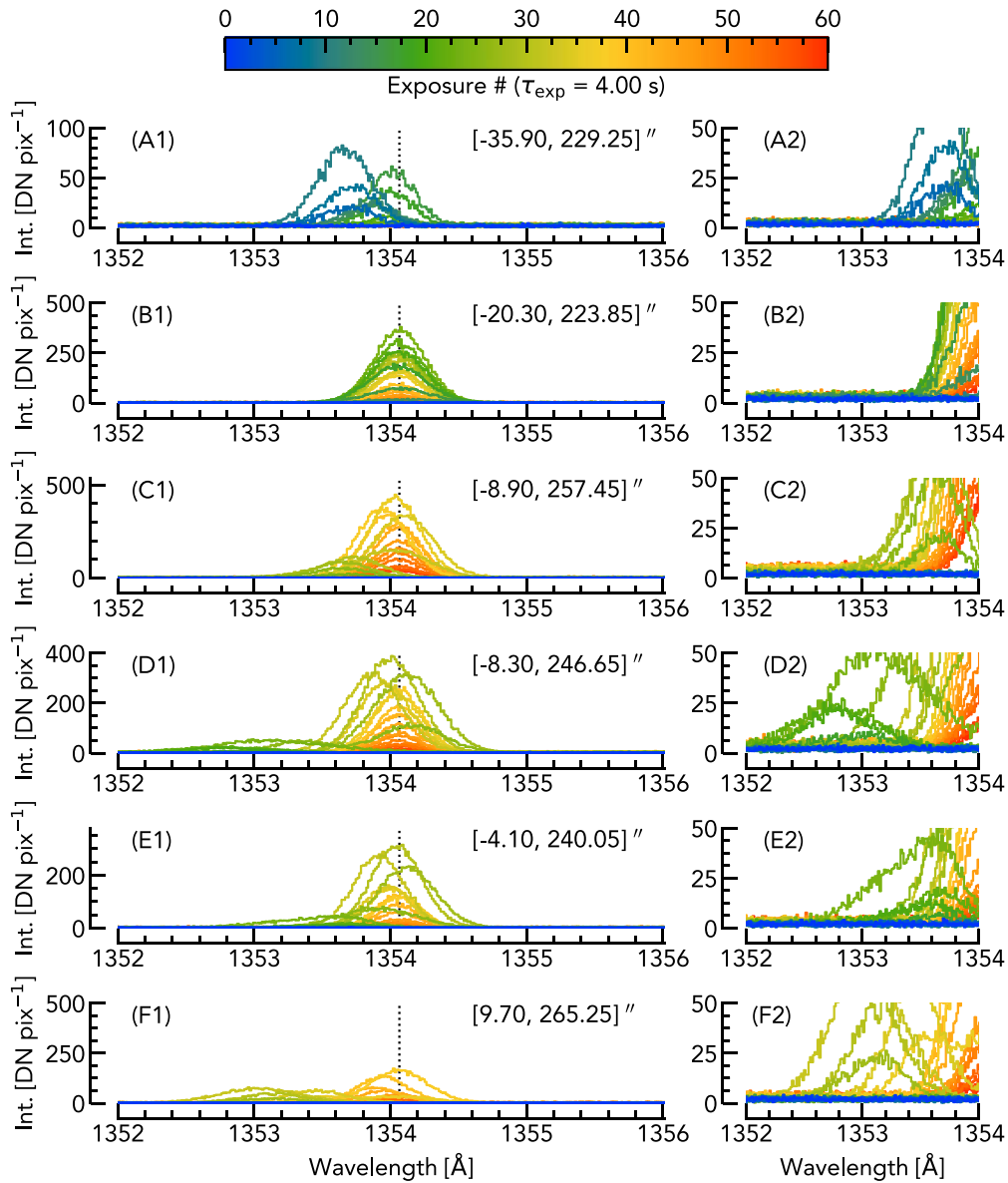


Figure 12. Sample Fe XXI line profiles from six pixels. Color represents exposure number (time). Exposures 0–60 are shown, in steps of two. Panels (A2)–(E2) show the same profiles, but zoomed in to see the weaker profiles in the initial impulsive phase of each pixel. An animation of this figure is available. The video begins at exposure zero and ends at exposure 60. The real-time duration of the video is 6 s.

(An animation of this figure is available.)

the footpoints before the loops are filled in following chromospheric ablation.

The magnitudes of these blueshifts are consistent with observations of Fe XXI and other high-temperature lines in flares, as is the morphology. Some small redshifts are present owing to the reflecting upper boundary condition of the loops and draining of flare loops. They are associated with the gradual phase of each loop and are small in magnitude.

Though the field-aligned simulation contains larger upflows than those suggested by the Fe XXI emission, the fastest upflows ($v > 400 \text{ km s}^{-1}$) occur in hotter plasma where there is little or no Fe XXI. There are also projection effects to take into consideration. The inclination of loops with respect to the line of sight affects the Doppler shift (and inferred upflow velocity). Even though each loop contained the same RADYN flare atmosphere, there was a range of Doppler shifts present, apparent from the animated version of Figure 15 and the superposed analysis presented in

Section 5.6. Having knowledge of the loop geometry can therefore be important for interpreting the Doppler shift results.

5.5. Synthetic Fe XXI Line Widths

The presence of line widths in excess of the quadrature sum of the thermal and instrumental widths is usually referred to as nonthermal broadening. There are several candidates that can cause nonthermal broadening. Our model accounts for two broadening mechanisms: thermal and superposition of loops. For thermal broadening we assume that the electron and ion temperatures are equal, and we assume statistical equilibrium since we used equilibrium ionization fractions in CHIANTI when calculating the contribution functions. If nonequilibrium ionization effects are significant and Fe XXI forms in hotter plasma assumed by statistical equilibrium, then we are likely underestimating thermal broadening.

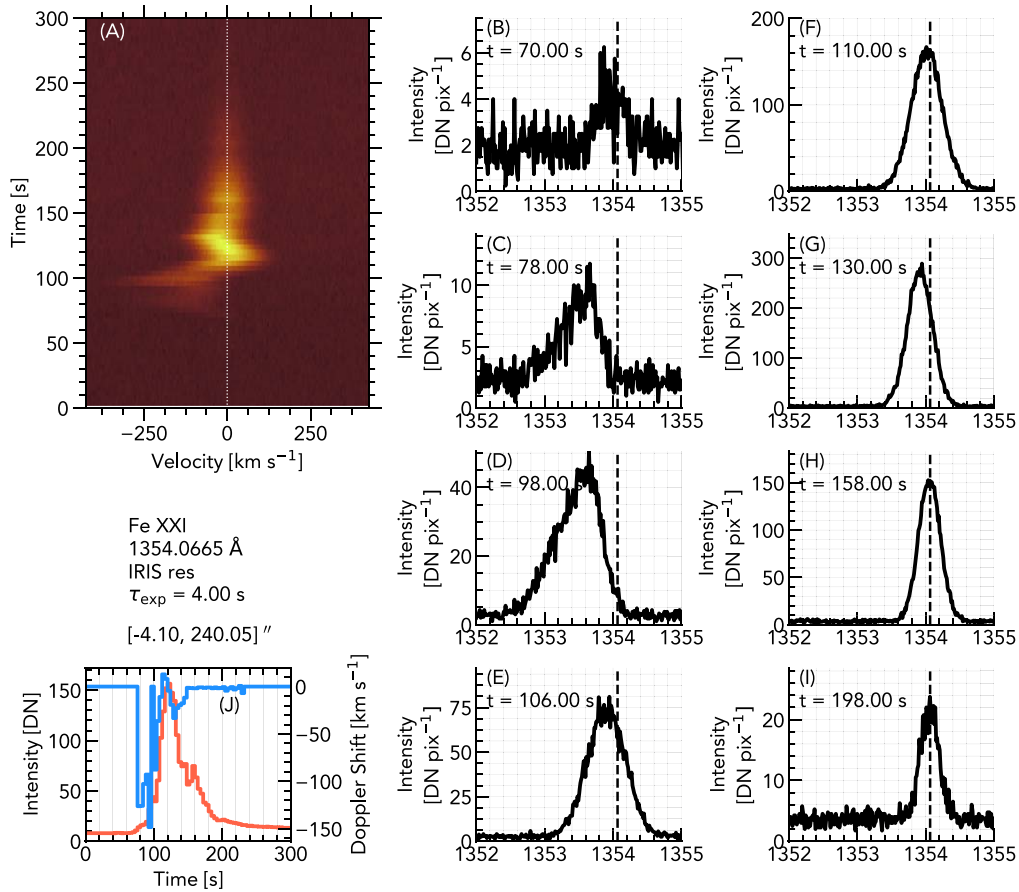


Figure 13. Detailed overview of a single pixel ($x = [-4.10, 240.05]''$). Temporal behavior is in panel (A), and individual profiles at various times are in panels (B)–(I). Light curves of intensity (orange) and Doppler shift (blue) are in panel (J).

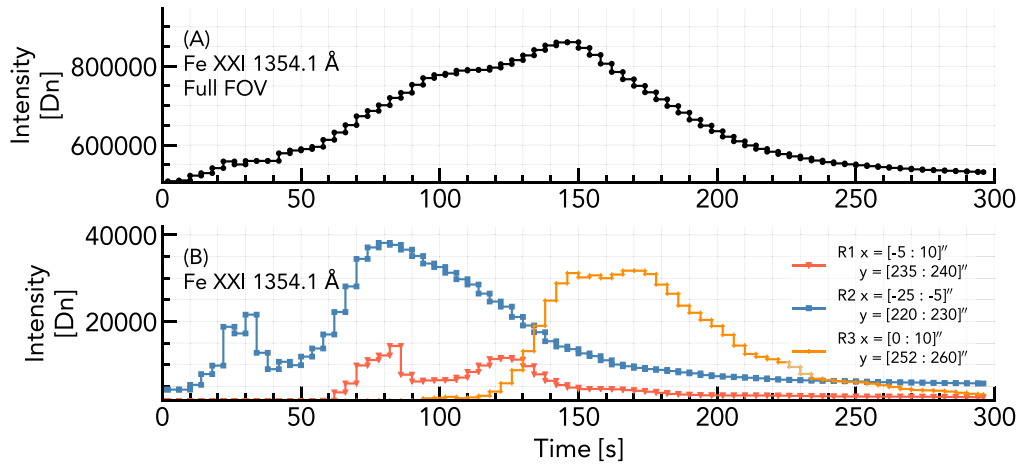


Figure 14. Fe XXI light curves from the full field of view (panel (A)) and from the three subregions (panel (B)) that are indicated in Figure 3.

Though Fe XXI has a contribution function peaking at 11.2 MK, density increases following ablation of material into the flare loop, which means that there can be sufficient EM at temperatures in excess of this peak to produce detectable emission. This would increase the width of the line beyond the nominal thermal width. Similarly, Fe XXI can form below this peak temperature, so that the line width may drop below the nominal thermal width. Using the temperatures at which $G(n_e, T) > G_{\text{peak}}/4$ as a guide, then a reasonable range of thermal widths can be on the order of

$T \sim [8.08\text{--}16.70]$ MK, $W_{\text{thm}} = [0.37\text{--}0.53]$ Å, $\sigma = [0.16\text{--}0.23]$, and $v_{\text{thm}} = [81.7\text{--}117.4]$ km s $^{-1}$.

Superposition of multiple sources along the line of sight is accounted for by our arcade model. This will increase the line width, as profiles experiencing different plasma motions will sum together. While this contributes toward enhanced line widths, this effect is likely to produce asymmetric profiles, unless viewing angles and loop geometry were unusually ideal. Indeed, Polito et al. (2019) demonstrated through loop

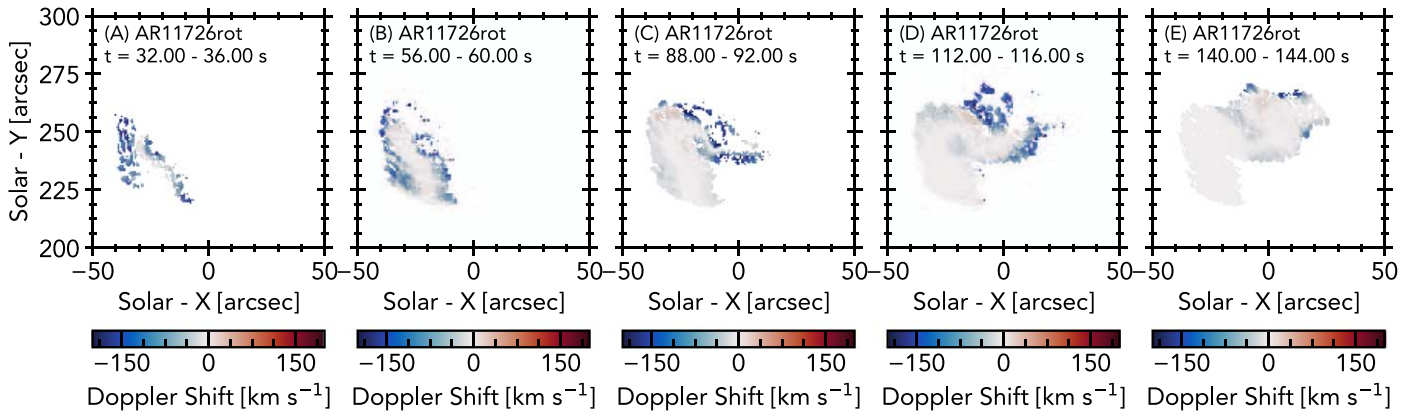


Figure 15. Dopplergrams of Fe XXI $\lambda 1354.0665$ emission at various snapshots in the flare arcade simulation of AR 11726rot. The background images are the integrated Fe XXI line intensities (scaled by $I^{1/4}$, and $\alpha = 0.1$), to place the derived Doppler shifts in context. An animation of this figure is available. The video begins in the $t = 0-4$ s bin and ends in the $t = 296-300$ s bin. The real-time duration of the video is 7 s.

(An animation of this figure is available.)

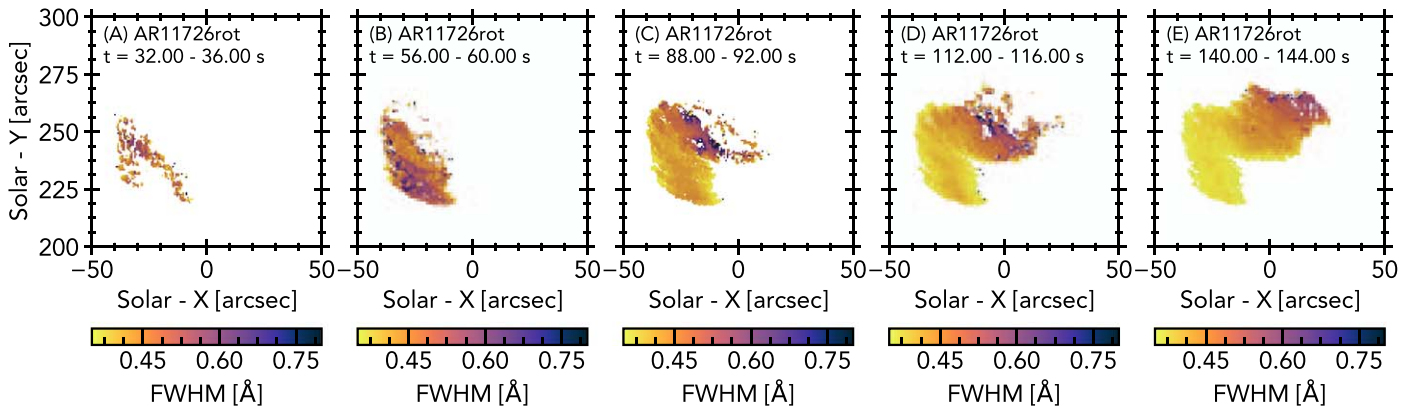


Figure 16. Maps of Fe XXI $\lambda 1354.0665$ FWHM, obtained from Gaussian fitting, at various snapshots in the flare arcade simulation of AR 11726rot. The background images are the integrated Fe XXI line intensities (scaled by $I^{1/4}$, and $\alpha = 0.25$), to place the derived line widths in context.

modeling that accounted for superposition of loops that this could broaden Fe XXI, but not symmetrically. They were unable to produce both very broad and symmetric profiles. Another broadening candidate would be required to explain the symmetry.

Gaussian FWHMs are shown in Figure 16. A movie is available online. From these maps it is clear that while some pixels exceed values of $W \sim [0.8-1]$ Å, the majority of profiles are broadened to values of $W \sim [0.5-0.6]$ Å only. Qualitatively these maps do show what we expect. The broadest profiles are near footpoints, with width decreasing through the flare loop.

Asymmetries, A_{RB} , were measured using the same approach as Polito et al. (2019) (and following De Pontieu et al. 2009; Tian et al. 2011). $A_{RB} = \frac{I_R - I_B}{I_P}$, where I_P is peak intensity, $I_{R/B} = \frac{\sum_{+/-\lambda_2} I_{\lambda} / n}{\sum_{+/-\lambda_1} I_{\lambda} / n}$, $\lambda_1 = 50 \text{ km s}^{-1}$, and $\lambda_2 = 150 \text{ km s}^{-1}$. Figure 17(a) shows the correlation between line width and asymmetry. While there is no strong correlation here (broad profiles can be both very asymmetric or symmetric), it is clear that when profiles are asymmetric they are broad, in agreement with Polito et al. (2019). In that figure color represents time since first detection. The broadest, more asymmetric profiles occur early in each loop. Maps of asymmetry show larger asymmetry in newly activated loops, when flows are strongest, consistent with observations analyzed by Imada et al. (2008) of cooler Fe XIV lines. Figure 17(b) shows the correlation

between line width and Doppler shift. While there is a relation, the correlation is not very strong, similar to observations of, e.g., Milligan (2011).

We have also not considered turbulence, broadening by Alfvénic waves, or nonequilibrium ionization (where Fe XXI could actually form in hotter plasma; e.g., Dudík et al. 2017), which will feature in follow-up work. Polito et al. (2019) contain a more detailed summary of potential nonthermal broadening mechanisms.

5.6. Synthetic Fe XXI Superposed Epoch Analysis

To characterize the response of all of the line profiles in the arcade simulation, a superposed epoch analysis was performed. This can highlight any commonalities between the response of individual sources and provide a statistical overview of the flare. Such an analysis can also be compared to observational examples presented in Figure 10 and in Graham & Cauzzi (2015).

The temporal origin of each pixel was the moment of first detection (first successful Gaussian fit to the data). This analysis was performed on the full flare (all flaring pixels) and separately on pixels identified as footpoints. Figure 18 shows the superposed epoch analysis where the left panels (A), (C), (E) are the full flare and the right panels (B), (D), (F) are footpoints only.

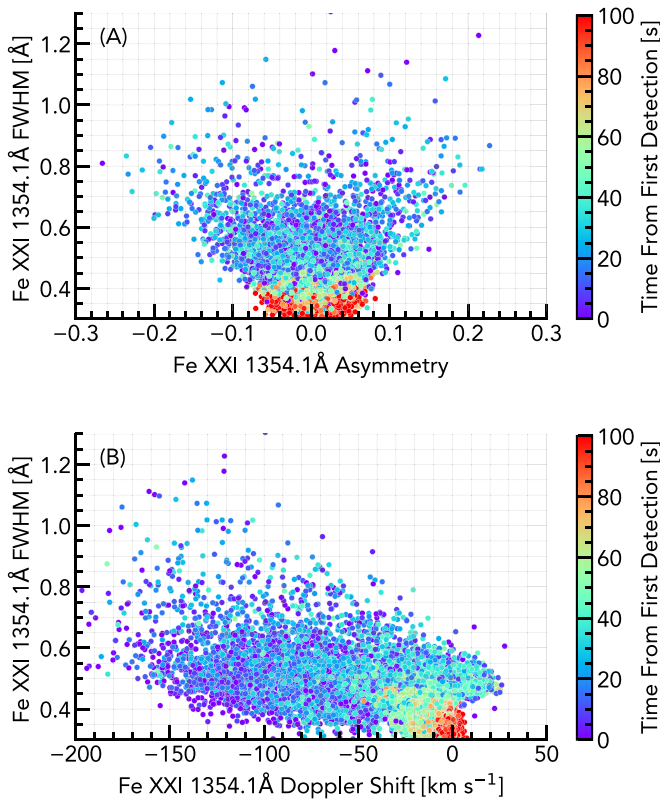


Figure 17. (A) Scatter of line width (FWHM) vs. asymmetry of the line, for AR 11726rot, and (B) scatter of line width (FWHM) vs. Doppler shift. Color represents time since the line was first present with sufficient signal to perform a Gaussian fit.

For all line properties the time bins were $\delta t = 4$ s. The integrated line intensity used a binning of $\delta I = 10$ DN pixel $^{-1}$, the Doppler shift used a binning of $\delta v = 10$ km s $^{-1}$, and the line widths used a binning of $\delta W = 12.5$ mÅ.

Our arcade model shows a larger spread of Doppler shifts than the observational analysis indicates. Further, observations have shown that blueshifts persist for several hundred seconds. In our model the Doppler shifts sharply decline over several tens of seconds and are only modest by hundreds. Footpoint sources have a somewhat more sustained blueshift than the arcade overall. Mass flows from pixels in the loops are smaller in magnitude and shorter in duration than those from the footpoint pixels. The temporal behavior of the line widths tracks that of the Doppler shifts. Footpoints exhibit an initially slower decay, followed by a decline to pre-flare values. When including loop and loop top sources, the decay is very smooth. Together, the larger spread of Doppler shifts and rapid cessation of Doppler shifts suggest that we are missing some aspect of the heating process (in either construction of the arcade or the underlying RADYN modeling).

As expected, the intensities take some time to peak relative to the Doppler shifts and line widths, about $t \sim 50$ s. The initial spikes there are due to the intense continuum in footpoint sources.

6. Summary and Conclusions

We have created a data-constrained flare arcade model by grafting the results of a state-of-the-art flare loop simulation onto observed active region loop structures. This bridges the gap between advanced 1D loop models that can capture the NLTE, nonlocal, radiation hydrodynamics on spatial scales

appropriate for flares, and 3D models that capture effects such as loop geometry, superposition of loops, and viewing angle on the solar disk. While this initial arcade model is rather simplified, it sets a framework for us to investigate both individual flare sources and the global and stellar flares.

Synthetic observables from SDO/AIA, GOES/XRS, and the IRIS spacecraft were forward modeled taking into account instrumental effects where appropriate. This illustrates the utility of this arcade model as a means to facilitate a more accurate model–data comparison for coronal emission in flares. Some specific summary points are as follows:

1. The morphological characteristics of flares are well represented by our arcade model. While increases in the EMs at temperatures in excess of >10 MK first appeared near loop tops, these were too small to produce observable SDO/AIA or IRIS radiation. Radiation sampling plasma >10 MK is therefore first observed near the footpoints of loops. Following ablation of material into the loop and loop tops, EMs became significantly stronger and radiation was observed in those locations. The synthetic AIA movies show the ablation process. As loops cool, they become visible in passbands that sample cooler plasma. The brightest emission is initially the footpoints/ribbons, switching to the post-flare loops in the gradual phase.
2. Synthetic GOES/XRS light curves were qualitatively similar to observations, with a steep, impulsive rise phase followed by a more gradual decay phase. The temperature and EM from GOES are what we would expect from flares. However, the decay timescales imply a very close ribbon distance (based on Reep & Toriumi 2017). Our model does not include ribbon separation or increasing loop length, both of which could lengthen the decay phase. Combined with synthetic AIA light curves, it is clear that the cooling timescale of our flare loops from RADYN is too rapid.
3. Synthetic Fe XXI emission also shows a qualitative match to observations, both the images and spectral behavior. The magnitude and location of Doppler shifts and line intensities were consistent with observations. However, the lifetime of Doppler shifts was too short. Compared to the observed superposed epoch analysis, there is a much larger spread of Doppler shifts in the model. Observations are instead tightly clustered. Though line broadening occurred, the line widths were too narrow, suggesting that additional physics is required in the model to broaden the lines.

Based on our experience running electron-beam-driven simulations (and that of others; see works referenced in Section 1), we do not believe that varying the nonthermal electron beam parameters (flux, low-energy cutoff, spectral index) will by themselves produce upflow durations more consistent with observations. Instead, the answer likely lies in the modeling approach, or in improvements to the physics of the model. Planned improvements over this initial work include modeling the loop structures and flare evolution from an actual flare, inclusion of ribbon separation, including varied loop lengths, varying the electron beam properties injected onto the loops, and performing multithreaded modeling (e.g., Reep et al. 2018a). Going beyond the standard model electron beam scenario, we will include return currents and proton beams

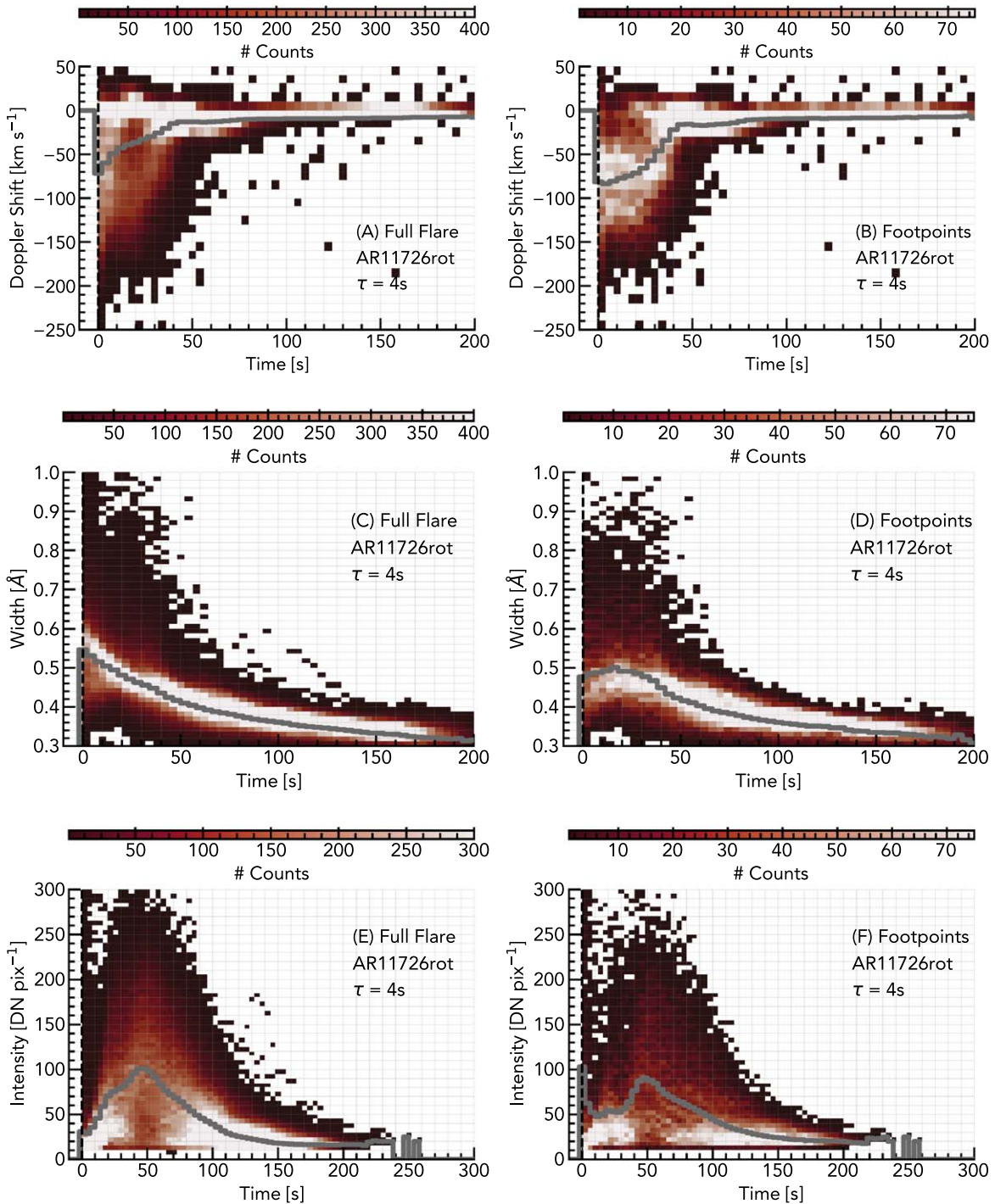


Figure 18. Superposed epoch analysis of Fe XXI line for the full flare (left column) and for footpoint sources only (right column). The first row is the Doppler shift, the second row is the line widths, and the third row is integrated line intensity. In each panel the weighted mean value is shown as a solid gray line.

(using the recently developed FP code merged with RADYN; J. C. Allred et al. 2020, in preparation).

Multithreaded modeling by Reep et al. (2018a) has been able to achieve Doppler shifts with durations more consistent with observations. However, this requires sustained energy injection (of 60–200 s) into a single atmospheric volume, over many individual threads within a single IRIS pixel. There is no clear explanation as to why energy deposition into one location would last this long, given reconnection timescales. Indeed, the timescales associated with redshifts of chromospheric spectral lines (chromospheric condensations) forward modeled in single-threaded RADYN

simulations show much closer consistency with observations than the timescales of upflows (e.g., Graham et al. 2020). Further, Graham et al. (2020) used IRIS ultraviolet observations to show that the energy injection timescale was on the order of ≈ 20 s. We therefore believe that, as well as pursuing a multithreaded approach, we should investigate the physics of the flare heating and cooling also.

Recent updates to nonthermal particle transport in RADYN include a self-consistent treatment of the beam-induced return current (J. C. Allred et al. 2020, in preparation). Initial results by J. C. Allred et al. (2020, in preparation) indicate that the

heating rates can be significantly modified by the return currents. Additionally, Emslie & Bian (2018) have showed that thermal conduction can be suppressed by turbulence and nonlocal effects and provided a mechanism to include this in a code such as RADYN. This could have implications for both flare impulsive and gradual phase dynamics and associated timescales. We have begun to adapt RADYN to include suppression of conduction. Post-impulsive phase heating has been suggested as an explanation for the longer-than-expected flare cooling times (e.g., Qiu & Longcope 2016; Zhu et al. 2018). This can be investigated in our simulations in combination with suppression of conduction.

With regard to line broadening, nonequilibrium ionization would result in a different Fe ionization stratification than that predicted by our assumption of ionization equilibrium. This could result in ions forming in plasma significantly hotter than the equilibrium formation temperatures, with a correspondingly larger thermal width. These effects can be investigated, for example, by using the minority species version of RADYN (Kerr et al. 2019b, 2019c) to obtain nonequilibrium Fe ion fractions, or by applying our framework with flare atmospheres from other codes, such as HYDRAD (Bradshaw & Mason 2003; Reep et al. 2019), that can model NEI ion fractions. Including ad hoc microturbulence and investigating the potential of broadening via Alfvénic waves (estimating broadening using the models of Kerr et al. 2016; Reep et al. 2018b) are other avenues to pursue, as suggested by Polito et al. (2019).

While we have used data-constrained loop structures here and plan to do this for a flaring active region, there is nothing to preclude our model being used with artificial loop structures either from a toy-model or originating from magnetohydrodynamic (MHD) flare and CME models. We would be keen to collaborate with MHD modelers, to simulate observables from those codes with the more accurate thermodynamics (and nonthermal particle beams) available from using RADYN and our arcade modeling approach.

G.S.K. was funded by an appointment to the NASA Postdoctoral Program at Goddard Space Flight Center, administered by USRA through a contract with NASA. J.C.A. acknowledges funding support from the Heliophysics Supporting Research and Heliophysics Innovation Fund programs. V.P. acknowledges support by NASA grant 80NSSC20K0716. IRIS is a NASA small explorer mission developed and operated by LMSAL with mission operations executed at NASA Ames Research center and major contributions to downlink communications funded by the Norwegian Space Center (NSC, Norway) through an ESA PRODEX contract. We thank Dr. J. Reep for assistance with the GOES-15 spectral responses. This research benefited from discussions held at a meeting of G.S.K.’s and V.P.’s International Space Science Institute team: “Interrogating Field-Aligned Solar Flare Models: Comparing, Contrasting and Improving.”

ORCID iDs

Graham S. Kerr  <https://orcid.org/0000-0001-5316-914X>
 Joel C. Allred  <https://orcid.org/0000-0003-4227-6809>
 Vanessa Polito  <https://orcid.org/0000-0002-4980-7126>

References

- Abbett, W. P., & Hawley, S. L. 1999, *ApJ*, 521, 906
 Allred, J., Daw, A., & Brosius, J. 2018, arXiv:1807.00763

- Allred, J. C., Hawley, S. L., Abbett, W. P., & Carlsson, M. 2005, *ApJ*, 630, 573
 Allred, J. C., Kowalski, A. F., & Carlsson, M. 2015, *ApJ*, 809, 104
 Aschwanden, M. J. 2013, *ApJ*, 763, 115
 Aschwanden, M. J. 2016, *ApJS*, 224, 25
 Aschwanden, M. J., & Peter, H. 2017, *ApJ*, 840, 4
 Asplund, M., Grevesse, N., Sauval, A. J., & Scott, P. 2009, *ARA&A*, 47, 481
 Bornmann, P. L. 1990, *ApJ*, 356, 733
 Bradshaw, S. J., & Cargill, P. J. 2013, *ApJ*, 770, 12
 Bradshaw, S. J., & Klimchuk, J. A. 2011, *ApJS*, 194, 26
 Bradshaw, S. J., & Klimchuk, J. A. 2015, *ApJ*, 811, 129
 Bradshaw, S. J., & Mason, H. E. 2003, *A&A*, 401, 699
 Brosius, J. W., Daw, A. N., & Rabin, D. M. 2014, *ApJ*, 790, 112
 Brown, J. C. 1971, *SoPh*, 18, 489
 Brown, S. A., Fletcher, L., Kerr, G. S., et al. 2018, *ApJ*, 862, 59
 Carlsson, M. 1998, in *Space Solar Physics: Theoretical and Observational Issues in the Context of the SOHO Mission*, ed. J. C. Vial, K. Bocchialini, & P. Boumier (Berlin: Springer)
 Carlsson, M., & Stein, R. F. 1992, *ApJL*, 397, L59
 Carlsson, M., & Stein, R. F. 1997, *ApJL*, 481, 500
 Carlsson, M., & Stein, R. F. 2002, *ApJ*, 572, 626
 Cheng, J. X., Kerr, G., & Qiu, J. 2012, *ApJ*, 744, 48
 Cheung, M. C. M., Rempel, M., Chintzoglou, G., et al. 2019, *NatAs*, 3, 160
 Culhane, J. L., Harra, L. K., James, A. M., et al. 2007, *SoPh*, 243, 19
 De Pontieu, B., McIntosh, S. W., Hansteen, V. H., & Schrijver, C. J. 2009, *ApJL*, 701, L1
 De Pontieu, B., Title, A. M., Lemen, J. R., et al. 2014, *SoPh*, 289, 2733
 Del Zanna, G., Dere, K. P., Young, P. R., Landi, E., & Mason, H. E. 2015, *A&A*, 582, A56
 Dennis, B. R., Phillips, K. J. H., Schwartz, R. A., et al. 2015, *ApJ*, 803, 67
 Dere, K. P., Landi, E., Mason, H. E., Monsignori Fossi, B. C., & Young, P. R. 1997, *A&AS*, 125, 149
 Dorfi, E. A., & Drury, L. O. 1987, *JCoPh*, 69, 175
 Doschek, G. A., Feldman, U., Dere, K. P., et al. 1975, *ApJL*, 196, L83
 Dudík, J., Džifčáková, E., Meyer-Vernet, N., et al. 2017, *SoPh*, 292, 100
 Emslie, A. G., & Bian, N. H. 2018, *ApJ*, 865, 67
 Feldman, U. 1992, *PhysS*, 46, 202
 Fisher, G. H. 1989, *ApJ*, 346, 1019
 Fisher, G. H., Canfield, R. C., & McClymont, A. N. 1985a, *ApJ*, 289, 425
 Fisher, G. H., Canfield, R. C., & McClymont, A. N. 1985b, *ApJ*, 289, 434
 Fletcher, L., Dennis, B. R., Hudson, H. S., et al. 2011, *SSRv*, 159, 19
 Fletcher, L., & Hudson, H. 2001, *SoPh*, 204, 69
 Fontenla, J. M., Avrett, E. H., & Loeser, R. 1993, *ApJ*, 406, 319
 Freeland, S. L., & Handy, B. N. 1998, *SoPh*, 182, 497
 Graham, D. R., & Cauzzi, G. 2015, *ApJL*, 807, L22
 Graham, D. R., Cauzzi, G., Zangrilli, L., et al. 2020, *ApJ*, 895, 6
 Grigis, P. C., & Benz, A. O. 2005, *ApJL*, 625, L143
 Holman, G. D. 2016, *JGRA*, 121, 11667
 Holman, G. D., Aschwanden, M. J., Aurass, H., et al. 2011, *SSRv*, 159, 107
 Imada, S., Hara, H., Watanabe, T., et al. 2008, *ApJL*, 679, L155
 Kašparová, J., Varady, M., Heinzel, P., Karlický, M., & Moravec, Z. 2009, *A&A*, 499, 923
 Kerr, G. S., Allred, J. C., & Carlsson, M. 2019a, *ApJ*, 883, 57
 Kerr, G. S., Carlsson, M., & Allred, J. C. 2019b, *ApJ*, 885, 119
 Kerr, G. S., Carlsson, M., Allred, J. C., Young, P. R., & Daw, A. N. 2019c, *ApJ*, 871, 23
 Kerr, G. S., Fletcher, L., Russell, A. J. B., & Allred, J. C. 2016, *ApJ*, 827, 101
 Kobayashi, K., Cirtain, J., Winebarger, A. R., et al. 2014, *SoPh*, 289, 4393
 Kontar, E. P., Brown, J. C., Emslie, A. G., et al. 2011, *SSRv*, 159, 301
 Kowalski, A. F., Allred, J. C., Daw, A., Cauzzi, G., & Carlsson, M. 2017, *ApJ*, 836, 12
 Kowalski, A. F., Hawley, S. L., Carlsson, M., et al. 2015, *SoPh*, 290, 3487
 Lemen, J. R., Title, A. M., Akin, D. J., et al. 2012, *SoPh*, 275, 17
 Magain, P. 1986, *A&A*, 163, 135
 Mandage, R. S., & Bradshaw, S. J. 2020, *ApJ*, 891, 122
 Mason, H. E., Shine, R. A., Gurman, J. B., & Harrison, R. A. 1986, *ApJ*, 309, 435
 Milligan, R. O. 2011, *ApJ*, 740, 70
 Milligan, R. O. 2015, *SoPh*, 290, 3399
 Narendranath, S., Sreekumar, P., Alha, L., et al. 2014, *SoPh*, 289, 1585
 Newton, E. K., Emslie, A. G., & Mariska, J. T. 1995, *ApJ*, 447, 915
 Pesnell, W. D., Thompson, B. J., & Chamberlin, P. C. 2012, *SoPh*, 275, 3
 Phillips, K. J. H., & Dennis, B. R. 2012, *ApJ*, 748, 52
 Polito, V., Reep, J. W., Reeves, K. K., et al. 2016, *ApJ*, 816, 89
 Polito, V., Reeves, K. K., Del Zanna, G., Golub, L., & Mason, H. E. 2015, *ApJ*, 803, 84
 Polito, V., Testa, P., Allred, J., et al. 2018, *ApJ*, 856, 178

- Polito, V., Testa, P., & De Pontieu, B. 2019, [ApJL](#), **879**, L17
- Procházka, O., Reid, A., Milligan, R. O., et al. 2018, [ApJ](#), **862**, 76
- Qiu, J., Liu, W., Hill, N., & Kazachenko, M. 2010, [ApJ](#), **725**, 319
- Qiu, J., & Longcope, D. W. 2016, [ApJ](#), **820**, 14
- Qiu, J., Longcope, D. W., Cassak, P. A., & Priest, E. R. 2017, [ApJ](#), **838**, 17
- Reep, J. W., Bradshaw, S. J., Crump, N. A., & Warren, H. P. 2019, [ApJ](#), **871**, 18
- Reep, J. W., Bradshaw, S. J., & Holman, G. D. 2016a, [ApJ](#), **818**, 44
- Reep, J. W., Bradshaw, S. J., & McAteer, R. T. J. 2013, [ApJ](#), **778**, 76
- Reep, J. W., Polito, V., Warren, H. P., & Crump, N. A. 2018a, [ApJ](#), **856**, 149
- Reep, J. W., & Russell, A. J. B. 2016, [ApJL](#), **818**, L20
- Reep, J. W., Russell, A. J. B., Tarr, L. A., & Leake, J. E. 2018b, [ApJ](#), **853**, 101
- Reep, J. W., & Toriumi, S. 2017, [ApJ](#), **851**, 4
- Reep, J. W., Warren, H. P., Crump, N. A., & Simões, P. J. A. 2016b, [ApJ](#), **827**, 145
- Ryan, D. F., Chamberlin, P. C., Milligan, R. O., & Gallagher, P. T. 2013, [ApJ](#), **778**, 68
- Ryan, D. F., Milligan, R. O., Gallagher, P. T., et al. 2012, [ApJS](#), **202**, 11
- Ryan, D. F., O'Flanagan, A. M., Aschwanden, M. J., & Gallagher, P. T. 2014, [SoPh](#), **289**, 2547
- Sadykov, V. M., Kosovichev, A. G., Kitiashvili, I. N., & Frolov, A. 2019, [ApJ](#), **874**, 19
- Sadykov, V. M., Vargas Dominguez, S., Kosovichev, A. G., et al. 2015, [ApJ](#), **805**, 167
- Schmelz, J. T., Reames, D. V., von Steiger, R., & Basu, S. 2012, [ApJ](#), **755**, 33
- Simões, P. J. A., Hudson, H. S., & Fletcher, L. 2015, [SoPh](#), **290**, 3625
- Smith, D. F., & Auer, L. H. 1980, [ApJ](#), **238**, 1126
- The SunPy Community, Barnes, W. T., Bobra, M. G., et al. 2020, [ApJ](#), **890**, 68
- Tian, H., Li, G., Reeves, K. K., et al. 2014, [ApJL](#), **797**, L14
- Tian, H., McIntosh, S. W., De Pontieu, B., et al. 2011, [ApJ](#), **738**, 18
- Tian, H., Young, P. R., Reeves, K. K., et al. 2015, [ApJ](#), **811**, 139
- Uitenbroek, H. 2001, [ApJ](#), **557**, 389
- Warren, H. P. 2014, [ApJL](#), **786**, L2
- White, S. M., Thomas, R. J., & Schwartz, R. A. 2005, [SoPh](#), **227**, 231
- Young, P. R., Tian, H., & Jaeggli, S. 2015, [ApJ](#), **799**, 218
- Zhu, C., Qiu, J., & Longcope, D. W. 2018, [ApJ](#), **856**, 27
- Zhu, Y., Kowalski, A. F., Tian, H., et al. 2019, [ApJ](#), **879**, 19